Microstructural characterization of zirconium carbide implanted with europium ions and annealed in a hydrogen atmosphere.

BY

Tshepiso Bridget Kadi

Submitted in partial fulfilment of the requirements for the degree of

MAGISTER SCIENTIAE

In the Faculty of Natural and Agricultural Sciences

University of Pretoria

December 2024

Supervisor: Dr T.T. Thabethe

Co-Supervisor: Dr D.F. Langa

Co-Supervisor: Dr T.P. Ntsoane

DECLARATION

I, Tshepiso Bridget Kadi, declare that the dissertation, which I hereby submit for the degree of MSc in University of Pretoria, is my own work and has not been submitted by for a degree at this or any other tertiary institution.

Signature: 

Date : 14/02/2025

Summary

Microstructural characterization of zirconium carbide implanted with europium ions and annealed in a hydrogen atmosphere.

BY

Tshepiso Bridget Kadi

Submitted in partial fulfilment of the requirements for the degree of (MSc) in Physics in the Faculty of Natural and Agricultural Science, University of Pretoria

Supervisor/Promotor: Dr T.T. Thabethe

Co-Supervisor: Dr D.F. Langa

Co-Supervisor: Dr T.P. Ntsoane

The rising global demand for electricity calls for sustainable energy solutions to reduce the environmental and health impacts of fossil fuels, which are major contributors to greenhouse gas emissions. Nuclear energy, recognized as a low-carbon alternative, has the potential to meet these demands due to its efficiency and lack of greenhouse gas emissions during energy production. Nuclear reactors such as High Temperature Gas-cooled Reactors (HTGRs) use the Tri-structural Isotropic (TRISO) fuel particles, where SiC acts as the main diffusion barrier for metallic fission products. Fission products like silver, strontium and europium have been observed to be released from the SiC layer. To address these issues and improve the high-temperature performance and fission product retention of the TRISO-coated fuel particles, a new material other than SiC is needed. The ZrC coating layer is a candidate to replace the SiC layer of the TRISO particle.

This study explores the effects of europium (Eu) ion implantation and subsequent annealing (600–800°C) on the microstructural and diffusion behavior of zirconium carbide (ZrC), a material of interest for advanced nuclear applications. The experimental findings were supported by SRIM simulations, which predicted a europium penetration depth of ~67 nm, closely aligning with RBS results showing a depth of ~76 nm. Ion implantation induced structural damage in ZrC, evident from reduced XRD peak intensities, increased full width at half maximum (FWHM), and indications of lattice strain and defects.

Thermal annealing significantly influenced Eu diffusion and ZrC's microstructure. At 700°C, RBS and EDS analyses showed that Eu ions migrated toward the surface, leading to localized enrichment of Eu and surface oxidation characterized by ZrO_2 formation. At 800°C, Eu diffusion extended outward, accompanied by broader RBS distributions and surface cracks visible in SEM images. These structural changes were linked to the thermal mobility of Eu ions and the oxidation-reduction dynamics in the hydrogen-rich annealing atmosphere, with partial oxide reduction observed at the higher annealing temperature.

Annealing also facilitated microstructural recovery, as evidenced by enhanced XRD peak intensities, increased crystallite sizes, and a reduction in dislocation density, indicative of recrystallization and improved lattice ordering. This recovery shows the potential of thermal treatments to repair implantation-induced damage and restore material integrity. In summary, this study provides a detailed understanding of the structural, compositional, and diffusion behaviors of Eu in ZrC following ion implantation and annealing. The findings highlight the critical role of thermal annealing in controlling ion mobility, surface oxidation, and lattice recovery, contributing to the development of ZrC for nuclear and other advanced material applications.

ACKNOWLEDGEMENTS

I would like to acknowledge the following people for their support and valuable contribution in the success of my study.

- My supervisor Dr T.T Thabethe for her patience, support, encouragement and invaluable guidance throughout this journey.
- My co-supervisors Dr T.P Ntsoane for his assistance with XRD measurements and guidance and Dr D.F Langa for his support and constructive feedback.
- Prof T.T Hlatshwayo for arranging beam time to run RBS measurements.
- Dr Z.A.Y Abdalla and Mr. T Mokgadi for their patience and guidance.
- I am deeply grateful to my family for their belief in my abilities which have been a source of strength during this difficult journey.
- My friend Tshegofatso Mashabela for his endless support.
- All the staff and fellow students in the Physics department for providing me with the resources and environment necessary to conduct this research.
- This work is based on the research supported in part by the National Research Foundation of South Africa (Ref Number: PMDS22070633824 and RA19112149344).
- The financial assistance of the NRF is hereby acknowledged. Opinions expressed and conclusions arrived at, are those of the author and not to be necessarily attributed to the NRF.

This dissertation would not have been possible without the contribution and support of these incredible individuals. Thank you all for being part of this journey.

TABLE OF CONTENTS

ABBREVIATIONS

CVD	Chemical Vapor Deposition
FP	Fission Products
EDS	Energy Dispersive X-ray Spectroscopy
GIXRD	Grazing incident X-ray Diffraction
HTGR	High Temperature Gas Cooled Reactors
RBS	Rutherford Backscattering Spectrometry
SEM	Scanning Electron Microscopy
SPS	Spark Plasma Sintering
SRIM	Stopping and Range of Ions in Matter
TRISO	Tri-structural Isotropic
XRD	X-ray Diffraction

Chapter 1 : Introduction

The need for electricity is growing at an exponential rate as the world becomes increasingly dependent on technology. Electricity is of importance to modern society as it powers not only our homes, but also businesses, transportation and extends to health care and education. Majority of the global energy needs are fulfilled by fossil fuels. Worldwide, it is evident that coal, stands as the primary contributor to electricity generation [1]. Long-term reliance on fossil fuels has serious negative effects on the environment (e.g. pollution, climate change etc.), human health and resource depletion [2,3,4]. When fossil fuels like coal burn in conventional power plants, greenhouse gases are released [5]. The energy sector is widely recognized as the primary source of greenhouse gas emissions, accounting for about 73% of global emissions [2,6]. The environmental and public health implications of fossil fuels have driven global interest in exploring energy sources with low carbon emissions.

Nuclear energy has emerged as a low carbon energy source because it does not generate greenhouse gases. It protects air quality by producing carbon-free electricity, eliminating pollution from burning fossil fuels. It is capable of meeting the world's energy demands due the amount of energy it releases [7,8]. It is a reliable energy source since it does not depend on weather conditions. Nuclear energy is not only limited to the generation of electricity, but it can also be used to power desalination plants, providing a large amount of energy needed to convert saltwater into drinkable water Additionally, nuclear energy can be harnessed for hydrogen production, which has various applications. [7]. Although it has many advantages, nuclear energy produces radioactive waste that remain hazardous for a long period of time. Storing this waste is a challenge and leaks from storage facilities could negatively impact the

environment and nearby residents. Despite strict safety regulations, the risk of nuclear accidents like core meltdown still exists. Disasters like Fukushima and Chernobyl demonstrate potential risk to both human health as well as the environment [9].

Nuclear energy is generated through the process of nuclear fission, where the nucleus of an atom splits (usually uranium), releasing energy, fission products, and neutrons. These released neutrons have the potential to trigger further fission reactions in other atoms [10,11]. A typical fission reaction proceeds according to the following equation [10]:

$$ {}^{1}_{0}n + {}^{235}_{92}U \rightarrow {}^{236}_{92}U \rightarrow {}^{140}_{55}Cs + {}^{93}_{37}Rb + 3({}^{1}_{0}n) \quad (1.1) $$

A large amount of energy in the form of heat is released from this reaction. The heat released from nuclear fission is transferred to a reactor coolant, which in turn heats water to produce high-pressure steam. This steam drives a turbine connected to a generator, where mechanical energy is converted into electrical energy. For every uranium atom that undergoes fission, approximately 200 MeV of energy is released [12]. This energy can be harnessed to produce electricity. This demonstrates that a nuclear power plant does not need constant fuel supply [12].

1.1 High Temperature Gas-cooled Reactors (HTGR) and Tristructural Isotropic (TRISO) particle

Safety is of most importance when putting a nuclear reactor into operation. The high temperature gas-cooled reactors (HTGRs) are designed to prioritize safety by using their inherent features to minimize the risk of plant conditions that may result in fuel failure and the

release of fission products [13]. The HTGRs use helium as a coolant, which is an inert fluid. This characteristic helps prevent chemical interactions between the fuel, moderator, and coolant. Figure 1.1 depicts the fuel used in the HTGR, which is a multilayered coated fuel particle known as the Tristructural isotropic (TRISO) fuel particle. The coated particle's roles are to produce energy and hold fission products. A uranium fuel kernel (UO_2 or UCO) enclosed by four distinct coating layers makes up the TRISO particle. Every layer of coating has a distinct purpose in maintaining the integrity of the coated particle. The porous pyrolytic carbon (PyC) known as the buffer layer, provides a void space which accommodates the release of gaseous fission products from the kernel, fuel swelling as well as fission recoils. The inner pyrolytic carbon layer (IPyC) has multiple functions, it acts as a seal layer to protect the kernel from the HCl byproduct of SiC layer deposition. Additionally, the IPyC provides a surface for the SiC layer to be deposited onto. Finally, it contributes to the retention of fission gases in the particle. The SiC coating layer, which is the main structural layer in the TRISO particle, provides mechanical strength for the particle. It also acts as a barrier to the diffusion of metallic fission products, which diffuse easily through the IPyC layer. The outer pyrolytic carbon (OPyC) layer protects and provides mechanical support for the SiC and also contains fission products in the event of failure of the SiC layer [14,15,16,17,18]. Coating layer properties and thicknesses can vary depending on the specific particle design and the fabrication processes [17].

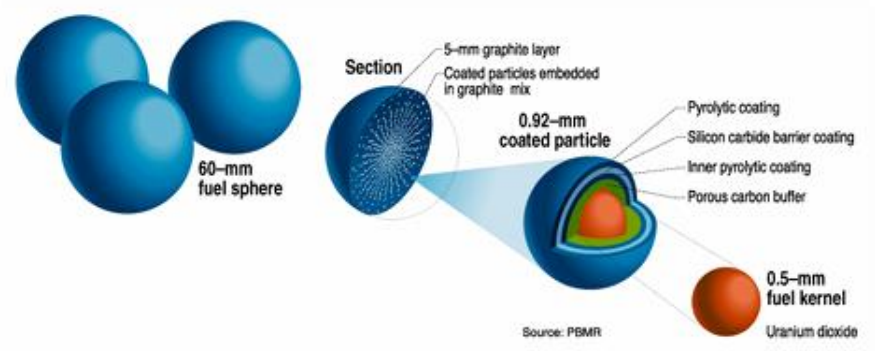

Figure 1.1: An illustration of the TRISO coated fuel particle in a pebble bed modular HTGR [19].

1.2 Europium

Europium (Eu) is a chemical element with atomic number 63 on the periodic table with a molar mass of 167.26 g/mol. Its electron configuration is $[Xe]4f^7 6s^2$. It is the most volatile member of the lanthanide series [20,21]. Although not naturally occurring in its free form, europium is commonly found within various minerals. It is a silvery metal with moderate hardness, it is highly reactive and readily oxidizes in air to form an oxide layer. It exhibits two oxidation states Eu^{2+} and Eu^{3+}. It undergoes a reaction with water that releases hydrogen gas. When exposed to air, it quickly oxidizes, potentially leading to combustion at temperatures between 150 – 180 ℃. The reactions of Eu with water and air occur as follows [22]:

$$2Eu_{(s)} + 3O_{2\,(g)} \rightarrow 2Eu_2O_{3\,(s)} \tag{1.2}$$

$$2Eu_{(s)} + 6H_2O_{(l)} \rightarrow 2Eu(OH)_{3\,(aq)} + 3H_2 \tag{1.3}$$

The stable isotopes of Eu are Eu-153 and Eu-151. Only four of its fourteen radioactive isotopes have longer half-lives, which makes them potentially dangerous. All other isotopes have half-lives of less than four months. The fission of Uranium or Plutonium produces these longer-

lived Eu isotopes (Eu- 152, Eu-154, and Eu-155). These isotopes have half-lives ranging from 5 to 13 years, and they decay by emitting a beta particle [21].

Europium is both externally and internally hazardous to human health. External exposure to europium-152 and europium-154 is concerning because of the strong gamma radiation linked to these two isotopes. A major health concern associated with europium is the increased likelihood of inducing cancer in the liver and bones [21].

1.3 Research Motivation

A TRISO particle is considered to have failed when the structural integrity of its protective layers is compromised, allowing the release of fission products. These failures can arise from various mechanisms, including fission product attack and the thermal decomposition of the silicon carbide (SiC) layer, which serves as the primary barrier to fission product migration [23]. Over time, fission products such as silver, strontium, and europium have been observed to diffuse through and escape from the SiC layer, significantly impacting the overall safety and performance of TRISO-coated fuel particles [24,25]. The degradation of the SiC layer is particularly concerning as it leads to a loss of containment, potentially increasing radiation exposure and contamination risks in high-temperature reactor environments [15].

Given the critical role of the SiC layer in TRISO fuel performance, extensive research has been directed toward improving its fission product retention and thermal stability [18]. However, despite its favorable properties, SiC remains susceptible to certain fission product interactions and degradation under extreme reactor conditions. To address these challenges and enhance the high-temperature performance of TRISO-coated fuel particles, alternative materials are

being explored as potential replacements for SiC [18]. Among these, zirconium carbide (ZrC) has emerged as a promising candidate due to its superior properties, including excellent thermal stability, enhanced resistance to fission product attack, and a low neutron absorption cross-section, which makes it particularly suitable for nuclear applications [16,23,26]. These advantages position ZrC as a safer and more effective material for use in next-generation TRISO fuel designs, leading to the development of ZrC-TRISO coated particles [18].

While ZrC presents several advantages over SiC, its long-term behavior under reactor conditions, particularly its interaction with fission products, remains an area of active investigation. Europium, one of the fission products known to be released from TRISO particles, poses a significant concern due to its potential to alter the microstructure and stability of the ZrC layer. Understanding the interaction between europium and ZrC is crucial for assessing the material's viability as a protective barrier in advanced nuclear fuels. This study aims to provide important information about the microstructural changes of ZrC in the presence of europium, contributing to the broader effort to enhance the safety, performance, and longevity of TRISO-coated fuel particles in high-temperature nuclear reactor environments.

1.4 Aims

This study is aimed at investigating:

1. The effect of Eu ion implantation and heat treatment on the microstructure of ZrC.
2. The diffusion behaviour of Eu ions in the ZrC substrate.

1.5 Objectives

To investigate the effects of europium ion implantation and subsequent annealing on ZrC samples, the study involved implanting europium ions at room temperature with a fluence of $1x10^{16}$ cm^{-1} and the energy of 360 keV. The samples were subsequently annealed at temperatures of 600℃, 700℃, and 800℃ in hydrogen gas. The surface morphology was analyzed using scanning electron microscopy (SEM). The elemental composition of the sample was determined using Energy Dispersive X-ray Spectroscopy (EDS). X-ray diffraction (XRD) was used to study the structural changes of the samples and Rutherford backscattering spectrometry (RBS) was used to study the diffusion behaviour of Eu within ZrC substrate.

1.6 Dissertation outline

This dissertation is composed of 8 chapters, each addressing different aspects of this study. Chapter 1 provides a background and information about the TRISO particle and HTGRs, as well as the production of the chosen fission product used in this research. Chapter 2 discusses the properties and synthesis of ZrC. In chapter 3 the process of ion implantation is discussed. Chapter 4 explores the different mechanisms of diffusion. Chapter 5 provides an overview of the research conducted on ZrC. The experimental procedure is outlined in chapter 6 which includes the sample preparation, annealing of the samples and the analysis techniques employed in this study. Chapter 7 presents the findings obtained. Chapter 8 concludes the dissertation with a summary of the key findings and recommendations for future research.

1.7 References

1. Ritchie, H., and Rosado, P. 2020. Electricity Mix. Our World in Data. Available at: https://ourworldindata.org/electricity-mix
2. Finkelman, R.B., Wolfe, A. and Hendryx, M.S., 2021. The future environmental and health impacts of coal. Energy Geoscience, 2(2), pp.99-112.
3. Barbir, F., Veziroğlu, T.N. and Plass Jr, H.J., 1990. Environmental damage due to fossil fuels use. International journal of hydrogen energy, 15(10), pp.739-749.
4. Gasparotto, J. and Martinello, K.D.B., 2021. Coal as an energy source and its impacts on human health. Energy Geoscience, 2(2), pp.113-120.
5. Myhrvold, N.P. and Caldeira, K., 2012. Greenhouse gases, climate change and the transition from coal to low-carbon electricity. Environmental Research Letters, 7(1), p.014019.
6. Haneklaus, N., Qvist, S., Gładysz, P. and Bartela, Ł., 2023. Why coal-fired power plants should get nuclear-ready. Energy, p.128169.
7. Brook, B.W., Alonso, A., Meneley, D.A., Misak, J., Blees, T. and van Erp, J.B., 2014. Why nuclear energy is sustainable and has to be part of the energy mix. Sustainable Materials and Technologies, 1, pp.8-16.
8. Da Mata, J.F., Neto, R.O. and Mesquita, A.Z., 2017. Comparison of the performance, advantages and disadvantages of nuclear power generation compared to other clean sources of electricity.
9. Gil, L., 2021. Recovering from a nuclear emergency: How Fukushima did it. IAEA Bulletin (Online), 62(1), pp.16-17.
10. United States. Department of Energy, 1993. DOE Fundamentals Handbook: Nuclear Physics and Reactor Theory. US Department of Energy.

11. Aref, L., Culligan, P.P.J., Czerwinski, K.R. and Nepf, H.M., 2018. Nuclear Energy: the Good, the Bad, and the Debatable. Massachusetts Institute of Technology. https://www.niehs.nih.gov/health/assets/docs_f_o/nuclear_energy_the_good_the_bad_and_the_debatable_508. pdf.
12. Lewis, E.E., 2008. Fundamentals of nuclear reactor physics. Elsevier.
13. Purba, J.H. and Tjahyani, D.T.S., 2019, April. A comparative study on safety design requirements between HTGR and LWR. In Journal of Physics: Conference Series (Vol. 1198, No. 2, p. 022020). IOP Publishing.
14. Gulden, T.D., Smith, C.L., Harmon, D.P. and Hudritsch, W.W., 1972. The mechanical design of TRISO-coated particle fuels for the large HTGR. Nuclear Technology, 16(1), pp.100-109.
15. Bing, L.I.U., LIANG, T. and Chunhe, T.A.N.G., 2006. A review of TRISO-coated particle nuclear fuel performance models. Rare Metals, 25(6), pp.337-342.
16. Zhou, X.W. and Tang, C.H., 2011. Current status and future development of coated fuel particles for high temperature gas-cooled reactors. Progress in Nuclear Energy, 53(2), pp.182-188.
17. Demkowicz, P.A., Liu, B. and Hunn, J.D., 2019. Coated particle fuel: Historical perspectives and current progress. Journal of Nuclear Materials, 515, pp.434-450.
18. Minato, K. and Ogawa, T., 2020. Advanced concepts in TRISO fuel.
19. Windes, W., Strydom, G., Kane, J. and Smith, R., 2014. Role of nuclear grade graphite in controlling oxidation in modular HTGRs (No. INL/EXT-14-31720). Idaho National Lab. (INL), Idaho Falls, ID (United States).
20. Ugale, A., Kalyani, T.N. and Dhoble, S.J., 2018. Potential of europium and samarium β-diketonates as red light emitters in organic light-emitting diodes. In Lanthanide-Based Multifunctional Materials (pp. 59-97). Elsevier.

21. Radioactive Properties of Key Europium Isotopes. (n.d.). [online] Available at: http://hpschapters.org/northcarolina/NSDS/europium.pdf (Accessed 04 June 2024)
22. Bashyal, J. 2024 Europium (EU) element: Reactions, properties, uses, effects, Science Info. Available at: https://scienceinfo.com/europium-eu-element-reactions/ (Accessed: 04 June 2024).
23. Minato, K., Ogawa, T., Sawa, K., Ishikawa, A., Tomita, T., Iida, S. and Sekino, H., 2000. Irradiation experiment on ZrC-coated fuel particles for high-temperature gas-cooled reactors. Nuclear Technology, 130(3), pp.272-281.
24. Verfondern, K., 1997. Fuel performance and fission product behaviour in gas-cooled reactor. IAEA-TECDOC-978.
25. Dwaraknath, S.S. and Was, G.S., 2016. The diffusion of cesium, strontium, and europium in silicon carbide. Journal of Nuclear Materials, 476, pp.155-167.
26. Katoh, Y., Vasudevamurthy, G., Nozawa, T. and Snead, L.L., 2013. Properties of zirconium carbide for nuclear fuel applications. Journal of Nuclear Materials, 441(1-3), pp.718-742.

Chapter 2 : The properties and synthesis of zirconium carbide (ZrC)

2.1 Zirconium Carbide

Zirconium carbide (ZrC) is a group IV transition metal carbide. It has an electron configuration of [Kr]5s24d2 and [He]2s22p3 [1]. It is a hard-crystalline refractory ceramic material. It has a metallic grey color and a face-centered cubic (fcc) cubic rock salt structure (Fm3m, space group 225). The Zr atoms are at the corners and centers of faces while the carbon atoms occupy the interstitial octahedral sites as illustrated in figure 2.1 [1,2,3]. The carbide can accommodate non-metal vacancies and are generally written with a non-stoichiometric formula $ZrC_{1-x,}$ where x represents carbon deficiency [1]. ZrC is often non-stoichiometric because it deviates from the ideal 1:1 Zr:C ratio.

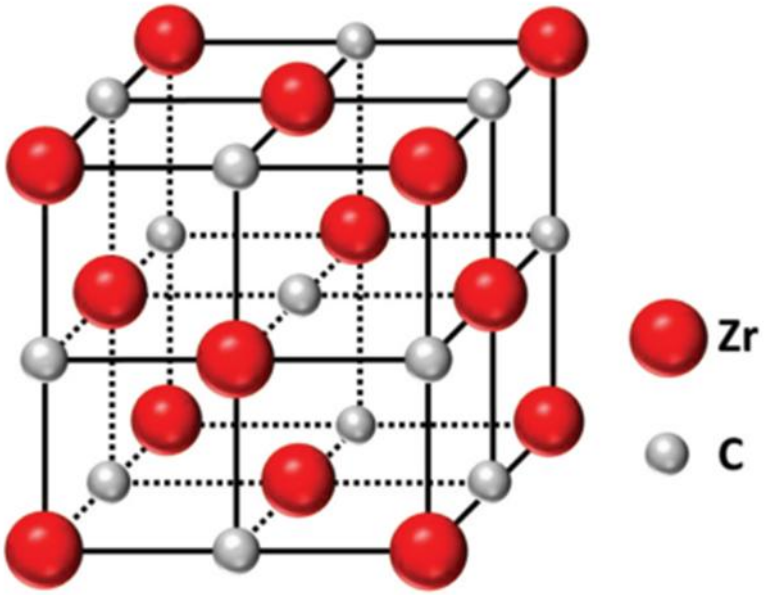

Figure 2.1: Crystal structure of ZrC [4].

The crystal structure of ZrC has a combination of ionic, covalent (Zr-C), and metallic (Zr-Zr) bonds. The C–Zr bonds are a combination of ionic and covalent bonds [5,6]. The ionic nature of the bonds is caused by the difference in electronegativity between the metal and non-metal [6,7]. Covalent bonding occurs between the 2p state electrons of carbon and the 4d state electrons of zirconium [6]. Metallic bonding arises when atoms are ionised, leaving the positive metal atoms and the delocalised electrons that move freely through the lattice [1]. In general, the metal-to-carbon (Zr-C) bond is known to be significantly stronger than the metal–metal bonds, as listed in table 2.1 [5]. A shorter bond length results in a stronger bond.

Table 2.1: Bond lengths of different types of bonds found in ZrC. [3,7,8].

Bond	**Bond Length (A)**
Zr-C	2.209
Zr-Zr	3.340
C-C	3.340

The different types of bonding in ZrC gives it a unique mixture of properties. ZrC has a high melting point of 3420˚C (melts without decomposition), high resistance to fission product attack, low neutron absorption cross sections [3,5]. It has high hardness, good thermal and electrical conductivity close to that of the Zr metal [2,6]. These attractive properties make ZrC a suitable candidate for ultra-high temperature applications [5,9]. It is important to note that fabrication methods may affect the properties of the material. Other physical properties of ZrC are listed in table 2.2.

Table 2.2: Characteristics and properties of ZrC [3,4,8,9].

Property/ Characteristic	**Value/Nature**
Structure	Cubic closed packed (fcc)
Color	Silver grey
Molecular Weight	104.91 g/mol
Lattice parameter	0.4698 nm
Density	6.59 g/cm^3
Melting point	3420˚C
Thermal conductivity	20.5 W/m·˚C
Thermal expansion	6.7×10^{-6}/˚C
Electrical Resistivity	$45\pm10\ \mu\Omega \cdot cm$
Vickers Hardness	25.5 GPa
Bond energy	83.6257 kJ/mol
Modulus of elasticity	350-440 GPa
Fracture toughness	2 MPa M$^{1/2}$
Bending strength	400 MPa

2.2 Synthesis of ZrC

ZrC can be synthesized through various methods, each contributing distinct attributes to the samples, influencing aspects such as their microscopic structure, chemical composition, and impurity levels. The synthesis techniques for ZrC encompass solid-phase reactions, solution-based precursors, and vapor-phase reactions [5,6,7].

2.2.1 Solid phase reactions

The most common method to synthesize zirconium carbide is through the carbothermal reduction of zirconia (ZrO_2) [3,5.7,10,11]. This is carried out at elevated temperatures between 2073-2873 K with a process time of 16 to 20 hours [5]. To ensure the purity of the final product, the reaction requires a carefully controlled environment, which is typically accomplished using a vacuum or inert gas. The reaction is an endothermic process which occurs according to the following equation [5,10,11]:

$$ZrO_{2(s)} + 3C_{(s)} \rightarrow ZrC_{(s)} + 2CO_{(g)} \quad (2.1)$$

This method often results in the presence of residual oxygen in the carbide lattice thus forming of a zirconium oxycarbide (ZrC_xO_y). Since ZrC is non-stoichiometric, the oxygen atoms could occupy the carbon vacancies or replace the carbon atoms to form an oxycarbide phase [11].

Equation 1 can be written in two steps, one showing the formation of the oxycarbide [6]:

$$ZrO_{2(s)} + C_{(s)} \rightarrow ZrC_xO_{y(s)} + CO_{(g)} \quad (2.2)$$

The oxycarbide then reacts with the remaining carbon to form ZrC.

$$ZrC_xO_{y(s)} + C_{(s)} \rightarrow ZrC_{(s)} + CO_{(g)} \quad (2.3)$$

To achieve the desired densities, grain sizes, and shapes in the final samples, the resulting zirconium carbide powder often undergoes additional high-temperature, extended-duration heat treatment processes [5].

The direct reaction of powdered zirconium or zirconium hydride with carbon is an additional way to synthesize ZrC. It falls under the category of combustion synthesis reaction [5,7]. The initial mixture of reactants is compressed to create a green body, which is then subjected to heating until it reaches the ignition temperature, the point at which the substance can start to combust. The reaction then releases enough heat to carry it through to the end. The reaction is carried out by the following equation:

$$Zr_{(s)} + C_{(s)} = ZrC_{(s)} \quad (2.4)$$

$$ZrH_{2(s)} + C_{(s)} = ZrC_{(s)} + H_{2(g)} \quad (2.5)$$

The Zr to C molar ratio, the applied external pressure, the initial green body density, and the specific surface area of the reactant particles all affect the final product's density. Achieving the desired densities, grain sizes, and shapes in the samples may necessitate prolonged sintering. The ability to produce relatively pure ZrC and shorter reaction times are the key benefits of this method.

2.2.2 Solution based precursors

Another method of producing ZrC is through solution-based precursors. The most common method for preparing ZrC is the sol-gel process. Wet chemical methods like sol-gel processing allow for much finer component mixing than is possible with conventional powder processing

[12]. Typically, Zr n-propoxide or zirconium oxychloride, along with a carbon source like alcohol or sugar, is employed to generate a polymer that includes Zr-O-Zr linkages [6]. Once the final product has been thoroughly dried, it is separated from the solvent and heated to start the carbothermic reaction. This approach requires additional steps to dry the mixture (about 24 hours) before starting the laborious carbothermic reduction reaction [5, 13]. Altering the ratio of the reactant precursors can produce ZrC with different stoichiometry.

2.2.3 Vapor phase reactions

Production of ZrC through vapor phase reactions has been a common practice for nuclear fuel coatings. Vapor deposition methods such as Chemical Vapor Deposition (CVD), evaporation and sputtering are used. CVD method is typically used in the production of Tri-structural Isotropic (TRISO) fuel particles [5,6].

The CVD method is used when a dense, homogeneous, and isotropic coating is needed. The exceptional throwing power of the CVD process is a defining characteristic that makes it possible to produce coatings with low porosity and uniform thickness and properties. Gaseous reactants are introduced into a reactor during each CVD process. The reaction occurs by the following general equation on a heated substrate surface.

$$Gaseous\ reactants_{(g)} \rightarrow Solid\ material_{(s)} + Gaseous\ product_{(g)} \qquad (2.6)$$

The process involves converting zirconium metal into a zirconium halide which is then reacted with a gaseous hydrocarbon like methane (CH_4). The reaction produces gaseous ZrC which is then deposited onto a suitable substrate. Zirconium halides like $ZrCl_4$, ZrI_4, and ZrB_4 are used

as gaseous ZrC precursors [5,6,7,15] This reaction is carried out at high temperatures between 1573-1773K and occurs according to the following equation [5,6]:

$$ZrX_4 + CH_4 + 2(1-X)H_2 \rightarrow ZrC_x + 4HX \quad (X = Cl, I, Br, x \leq 1) \tag{2.7}$$

The reaction occurs in an inert environment to avoid oxygen and other gaseous impurities. The stoichiometry of ZrC can be controlled by varying the mixture of the hydrocarbon [5].

2.3 ZrC phase diagram

Figure 2.2 illustrates a phase diagram for ZrC. It illustrates various phases present in the ZrC. The phase diagram exists for an atomic percent carbon range of 0-100% and a temperature range of 773-4273 K. At atomic percent carbon of 0 to 38.5 and temperature range of 773-1200K, there exists a hexagonal close packed Zr phase (α-Zr). At 1200-2127K, the previously observed α-Zr phase becomes a body centred cubic (β-Zr). The β-Zr begins to melt at temperatures above 2127K, thus forming a liquid Zr phase. At atomic percent carbon of 38.5-49.5% exists ZrC_x phase, where x is between 0.6 and 0.98. The melting point of this phase is 3723K. Beyond atomic percent carbon of 49.5, there exists ZrC_x + C phases. From the phase diagram it is seen that ZrC_x phase does not form a fixed 1:1 stoichiometry nor does it exist where $x > 1$. This means some carbon sites in the ZrC lattice. Are vacant. This phase diagram emphasizes the non-stoichiometric character of ZrC, its high-temperature stability, and phase boundaries.

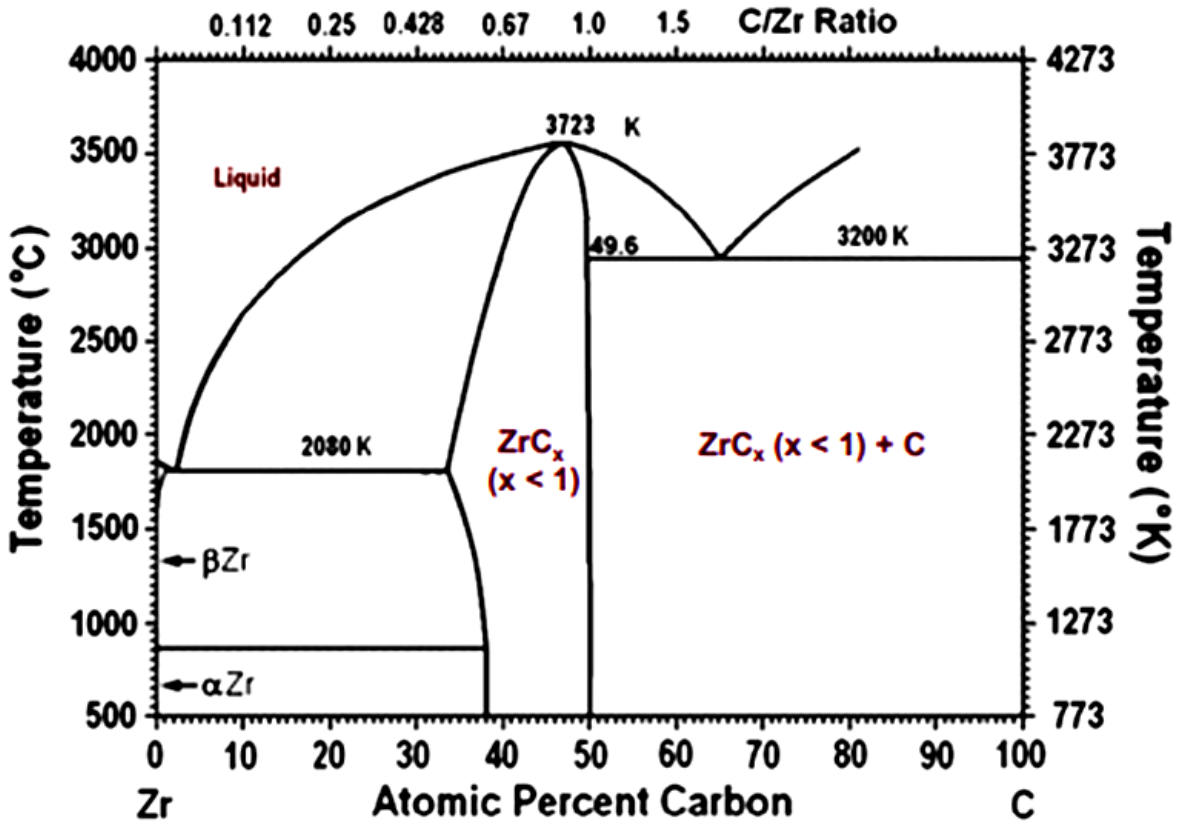

Figure 2.2: Phase diagram of ZrC [5].

2.4 References

1. Harrison, R.W. and Lee, W.E., 2016. Processing and properties of ZrC, ZrN and ZrCN ceramics: a review. Advances in Applied Ceramics, 115(5), pp.294-307.
2. Ul-Hamid, A., 2020. Microstructure, properties and applications of Zr-carbide, Zr-nitride and Zr-carbonitride coatings: A review. Materials Advances, 1(5), pp.1012-1037.
3. Pierson, H.O., 1996. Handbook of refractory carbides and nitrides: properties, characteristics, processing and applications. William Andrew.
4. Cui, K., Mao, H., Zhang, Y., Wang, J., Wang, H., Tan, T. and Fu, T., 2022. Microstructure, mechanical properties, and reinforcement mechanism of carbide toughened ZrC-based ultra-high temperature ceramics: A review. Composite Interfaces, 29(7), pp.729-748.
5. Katoh, Y., Vasudevamurthy, G., Nozawa, T. and Snead, L.L., 2013. Properties of zirconium carbide for nuclear fuel applications. Journal of Nuclear Materials, 441(1-3), pp.718-742.
6. Korklan, N.M., 2020. Intrinsic mechanical properties of zirconium carbide ceramics. Missouri University of Science and Technology.
7. Biira, S., 2017. Construction of a chemical vapour deposition reactor and the deposition of ZrC layers (Doctoral dissertation, University of Pretoria).
8. Yang, X.Y., Lu, Y., Zheng, F.W. and Zhang, P., 2015. Mechanical, electronic, and thermodynamic properties of zirconium carbide from first-principles calculations. Chinese Physics B, 24(11), p.116301.

9. Feng, L., Fahrenholtz, W.G., Hilmas, G.E., Watts, J. and Zhou, Y., 2019. Densification, microstructure, and mechanical properties of ZrC–SiC ceramics. Journal of the American Ceramic Society, 102(10), pp.5786-5795.
10. Maitre, A. and Lefort, P., 1997. Solid state reaction of zirconia with carbon. Solid State Ionics, 104(1-2), pp.109-122.
11. Gendre, M., Maître, A. and Trolliard, G., 2011. Synthesis of zirconium oxycarbide (ZrCxOy) powders: Influence of stoichiometry on densification kinetics during spark plasma sintering and on mechanical properties. Journal of the European Ceramic Society, 31(13), pp.2377-2385.
12. Ang, C., Williams, T., Seeber, A., Wang, H. and Cheng, Y.B., 2013. Synthesis and evolution of zirconium carbide via sol–gel route: features of nanoparticle oxide–carbon reactions. Journal of the American Ceramic Society, 96(4), pp.1099-1106.
13. Sacks, M.D., Bozkurt, N. and Scheiffele, G.W., 1991. Fabrication of mullite and mullite-matrix composites by transient viscous sintering of composite powders. Journal of the American Ceramic Society, 74(10), pp.2428-2437.
14. Carlsson, J.O. and Martin, P.M., 2010. Chemical vapor deposition. In Handbook of Deposition Technologies for films and coatings (pp. 314-363). William Andrew Publishing.
15. Ikawa, K., 1972. Vapor deposition of zirconium carbide-carbon composites by the iodide process. Journal of the Less Common Metals, 27(3), pp.325-332.

Chapter 3 : Ion Implantation

Ion implantation is a process whereby certain ions are introduced into the near-surface regions of a material in the form of an accelerated beam of ions as shown in figure 3.1. The energy used normally lies between 10 keV and 500 keV with corresponding penetrations ranging from 100 Å to 1 μm [1].

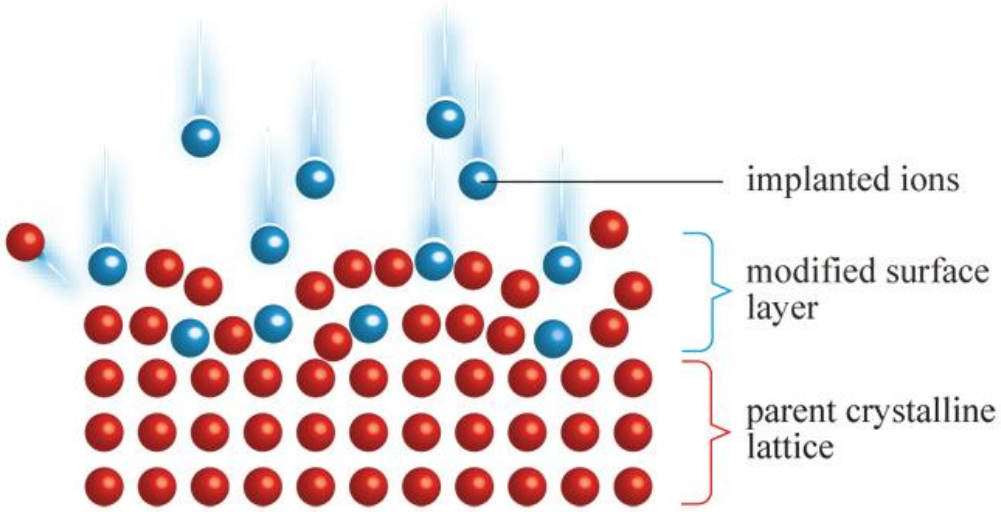

Figure 3.1: Representation of ions implanted into a substrate [2].

During ion implantation, ions are generated from a source material and separated to select the desired species. The process begins with introducing a material containing the desired elements into an ion source, where it is ionized, creating a mixture of ions (see figure 3.1). These ions are extracted from the ion source using an electric field, which accelerates them to form a beam of charged particles. The ion beam then passes through a mass analyzer, typically employing a magnetic field. The magnetic field deflects the ions according to their mass-to-charge ratio, allowing only the desired ions to pass through an aperture. After selection, the ion beam is

focused and shaped using a combination of electric and magnetic lenses. The selected ions are then further accelerated to high velocities using an electric field. Finally, the high-energy ions are directed into the target material, where they penetrate the surface and embed themselves into the lattice structure. This process allows for precise modification of the target material's properties [3]. When an energetic ion strikes a target, there is a rapid energy transfer to the target atoms. This results in various effects such as lattice structure disorder (radiation damage), surface atom ejection (sputtering), and ions finally become embedded into the target [4]. This can lead to noticeable changes in the chemical, physical, and mechanical properties of the sample's near-surface region [5]. These changes include formation or removal of phases, modification of the materials' surface and structural modifications such as the introduction of defects.

3.1 Ion Stopping

The stopping power plays a crucial role as ions traverse through materials, determining the amount of energy an ion loses per unit path length while penetrating a target. When energetic ions penetrate the target surface, a sequence of screened Coulomb interactions takes place. There are two energy loss mechanisms that exist: nuclear stopping and electronic stopping. The interaction of the ion with the target nuclei is called nuclear stopping and the interaction of the ion with the electrons of the target is called electronic stopping. The total stopping power is given by the sum of the nuclear and electronic stopping powers. Equation 3.1 illustrates the division of the ion's energy into two stopping parameters: nuclear stopping and electronic stopping [6].

$$\frac{dE}{dx} = \left.\frac{dE}{dx}\right|_n + \left.\frac{dE}{dx}\right|_e \tag{3.1}$$

Where subscripts n and e denote nuclear and electronic collisions, respectively.

Nuclear collisions (nuclear stopping) can involve large discrete energy losses and significant angular deflection of the trajectory of the ion. This process is responsible for the production of lattice disorder by the displacement of atoms from their positions in the lattice. Significantly less energy is lost in an electronic collision (electronic stopping), and there is very little lattice disorder and ion trajectory deflection. Figure 3.2 shows how the relative importance of the two energy-loss mechanisms changes rapidly with energy E and atomic number Z_1 of the particle [7]. Both stopping powers initially increase linearly to reach a maximum and then decrease thereafter.

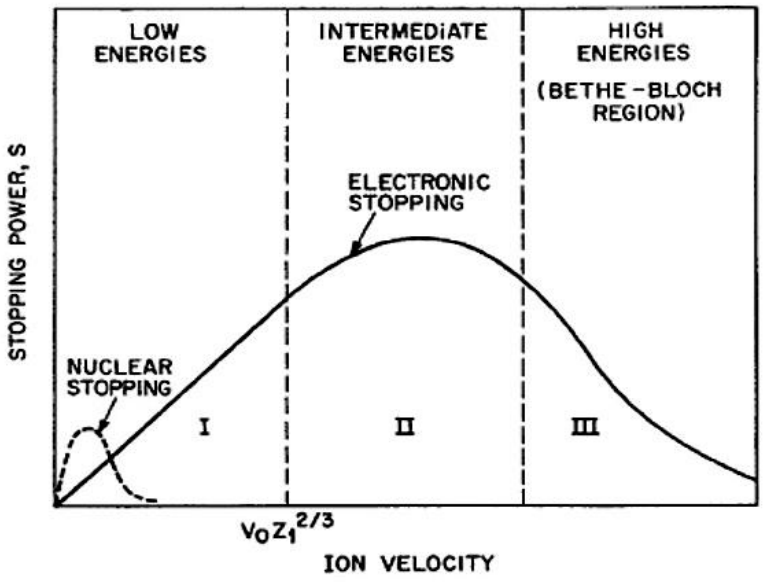

Figure 3.2: Nuclear and electronic components of the ion stopping power as a function of velocity [8].

3.1.1 Nuclear stopping

Nuclear stopping is concerned with the energy loss that results from elastic collisions between the incoming ion and the target. This energy loss mechanism dominates at low energies E and high ion atomic number Z_1 (see figure 3.2). A deeper analysis of the interactions between the two atoms is possible when the electrons are removed, leaving only the positively charged nuclei. The Coulombic potential between the two nuclei at a distance r can be determined using equation 3.2.

$$V_c(r) = \frac{e^2 Z_1 Z_2}{4\pi\varepsilon_0 r} \tag{3.2}$$

Where Z_1 and Z_2 are the atomic numbers of the ion and target respectively, e is the electron charge, ε_0 is the permittivity of free space $\left(\varepsilon_0 = 8.86 \times 10^{-14}\, {}^{F}/_{cm}\right)$ and r is the interatomic distance. In actuality, electrons surrounding atomic nuclei act as a screen barrier that reduces the effective nuclear charge. To account for this screening effect, a screening function denoted as $f_s(r)$needs to be included such that:

$$V(r) = V_c(r) f_s(r) \tag{3.3}$$

The collision between the ion and the target can be described by a two-body system considering the conservation of energy and momentum as illustrated in figure 3.3. As a result of the collision between M_1 and M_2, kinetic energy T is transferred. The value if T can be calculated using equation 3.4.

$$T = \frac{4M_1M_2}{(M_1 + M_2)} E sin^2\left(\frac{\theta}{2}\right) \tag{3.4}$$

where T is the energy lost by the incoming ion, E is the energy of the ion, M_1 and M_2 are the atomic masses of the ion and target respectively, and θ is the scattering angle.

One can compute the rate of energy loss due to nuclear collisions per unit path length by multiplying the energy loss by the likelihood of the collision happening. If the maximum possible energy transfer in a collision is T_{max} and there are N target atoms per unit volume, then:

$$S_n = \left(\frac{dE}{dx}\right)_{nuclear} = N \int_0^{Tmax} T d\sigma \tag{3.5}$$

where dσ is the differential cross section. Due to the elastic nature of nuclear stopping, energy lost by the incoming ion is transferred to the target atom that is subsequently recoiled away from its lattice site, thus creating a damage or defect site [3].

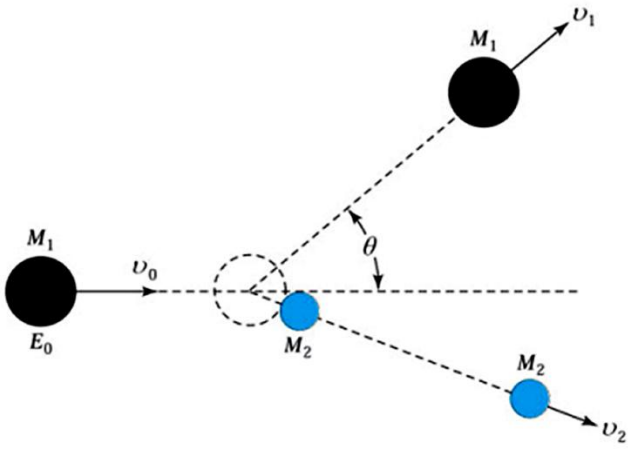

Figure 3.3: An illustration of elastic collision between the ion and target atom [9].

3.1.2 Electronic stopping

Electronic stopping results from the inelastic interaction between the incoming ion and the electrons within the target, leading to the excitation or ionization of atoms. Based on the ion's velocity, electronic stopping power can be classified into three regions (illustrated in figure 3.2). It dominates at high energy E and low Z_1.

In the first region (low energies), ions are moving with a velocity $\left(v < v_0 Z_1^{2/3}\right)$. In this velocity regime, many of the target electrons are moving much faster than the ions. This high electron velocity makes it difficult for the electrons to gain energy through direct collisions with the ions. In region II (intermediate energies), the velocities of the ions are of a magnitude comparable to Bohr's velocity $v \approx v_0 Z_1^{2/3}$. In this region, electronic stopping reaches its peak. In region III (high energies) also known as the Bethe-Bloch region, the incident ion becomes fully stripped of its electrons. At this point, the ion can be viewed as a positive point charge Z_1. This positive point charge is moving at a greater velocity than the average velocity of the electrons that orbit the shells of the target. The dynamics of energy transfer between ions and electrons change based on their relative velocities [7,10,11]. In region III, the energy loss is given by equation 3.6 [12].

$$-\left.\frac{dE}{dx}\right|_e = \frac{2\pi Z_1^2 e^4}{E} N Z_2 \left(\frac{M_1}{m_e}\right) \ln \frac{2 m_e v^2}{I} \tag{3.6}$$

where N is the atomic density, M_1 is the mass of the incident ion, m_e is the mass of the electron and I is the average excitation energy in eV and is given by equation 3.7.

$$I \cong 10Z_2 \tag{3.7}$$

where Z_2 is the atomic number of the stopping atoms.

3.2 Range and Range distribution

When an energetic ion is penetrating a target, it will go through collisions with the target nuclei and electrons, lose its energy and finally come to rest. The total distance an ion travels before it comes to rest is called the range, R. The ion's net penetration into the material, measured along the vector of the ion's incident trajectory, which is perpendicular to the surface in this example, is called the projected range, R_p. Both these quantities are illustrated in figure 3.4. As the occurrences of collisions per unit distance and the energy lost per collision are random variables, there will exist a spatial distribution of ions with identical mass and initial energy. The variations in the expected range are termed as the projected straggle σ_p or ΔR_p. Additionally, there is a statistical fluctuation occurring perpendicular to the axis of incidence, known as the lateral straggle $\sigma\perp$ [9,13,14]. Along the axis of incidence, the concentration of implants can be approximated by a Gaussian distribution function. Equation 3.8 provides the ion concentration as a function of depth [7,8,9].

$$n(x) = \frac{\phi}{\Delta R_p \sqrt{2\pi}} \cdot exp\left(-\frac{(x - R_p)^2}{2 \cdot \Delta R_p^2}\right) \tag{3.8}$$

where $n(x)$ is the ion concentration at depth x, ϕ is the ion implantation dose, R_p is the projected range and ΔR_p is the average deviation from the projected range.

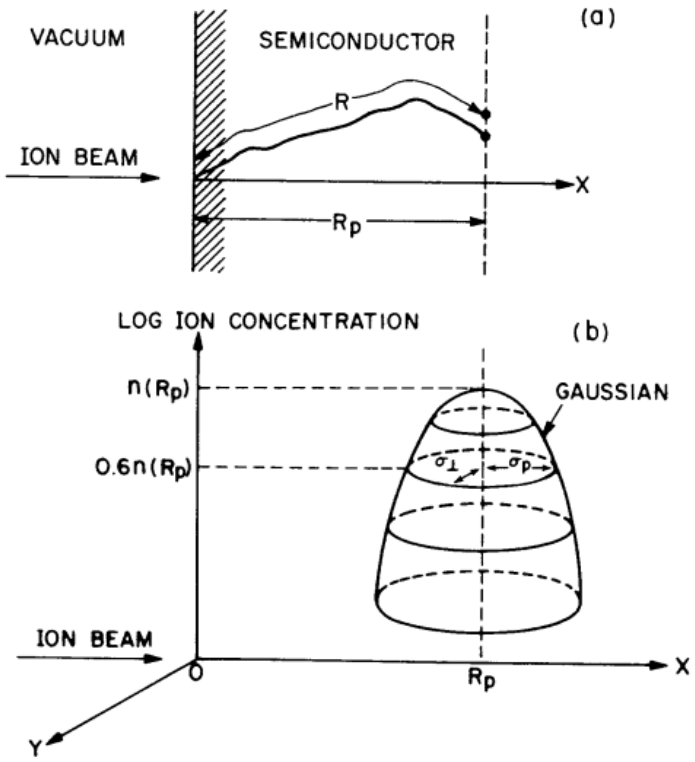

Figure 3.4: (a) A schematic representation of the ion range R and the projected range R_p. (b) A 2D distribution of the implanted ions [3].

3.3 Stopping and Range of Ions in Matter (SRIM) simulation

The Stopping and Range of Ions in Matter (SRIM) formerly known as TRIM [15,16] is a Monte-Carlo simulation that calculates the interaction of energetic ions with targets. SRIM is widely used to simulate ion implantation distributions and damage in a target. TRIM can handle complex targets composed of compound materials featuring up to eight layers, each comprising distinct materials. It can help determine radiation damage exposure (dpa). The software doesn't consider the crystal structure of dynamic composition changes in the material as ions penetrate it. SRIM achieves efficiency by simplifying ion-solid interactions through different approximations. Some of these approximations are:

- Binary collisions: The program focuses only on direct collisions between the incident ion and the target.
- Recombination of knocked off atoms: The program does not account for recombination of knocked off atoms with vacancies in the crystal lattice.
- Electronic stopping power: SRIM uses an average fit from several experiments to approximate the electronic stopping power.
- Interatomic potential: The interatomic potential is simplified to a universal form based on averaging fits to quantum mechanical calculations.
- Surface sputtering: If the target atom reaching the surface has enough momentum and energy, it can leave the surface.
- Layered system: The program does not simulate materials with composition differences in 2D or 3D.

There are two commonly used options for SRIM simulations; (1) Ion distribution and quick calculation damage and (2) detailed calculation with full damage cascades [16]. When using the first option, the damage calculated will be quick statistical estimates. The second option provides detailed information about the energy of every atom that gets displaced due to the collision with the incoming ions. The software is capable of computing the ultimate 3D ion distribution as well as various kinetic phenomena related to the ion's energy loss, including target damage, sputtering, ionization, and phonon production. Detailed tracking of all target atom cascades within the target is possible [15].

In this study, SRIM was utilized to model the implantation of Europium (Eu) ions onto Zirconium carbide (ZrC). The simulation was carried out in full cascade damage mode, with

the energy of 360 KeV for Eu ions. The displacement energies of 25 and 28 eV were used for Zr and C atoms respectively. The simulated outcomes were subsequently compared with experimentally obtained RBS data. Unlike SRIM, which is a simulation tool, RBS is an experimental technique used to analyze the elemental composition, depth profile and thickness of a material.

3.4 References

1. Dearnaley, G., 1975. Ion implantation. Nature, 256(5520), pp.701-705.
2. Prokhorov, A.M., 1990. Ion implantation. Physical encyclopaedia (Vol. 2, pp. 197-199). Russia.
3. City University of Hong Kong., (n.d.). City University of Hong Kong. [online] Available at: http://www.cityu.edu.hk. (28 October 2023)
4. Townsend, P.D., 1986. Ion implantation—an introduction. Contemporary physics, 27(3), pp.241-256.
5. Page, T.F., 1991. Ion implantation. In Concise Encyclopedia of Advanced Ceramic Materials (pp. 252-257). Pergamon.
6. Adhikari, G.P. and Limbu, H.K., 2019. Damage formation and calculation of energy loss during implantation of antimony and boron ion in silicon target. Journal of Nepal Physical Society, 5(1), pp.103-110.
7. Nastasi, M.A. and Mayer, J.W., 2006. Ion implantation and synthesis of materials (Vol. 5, pp. 63-76). Berlin: Springer.
8. Machaka, R., 2008. Ion Beam Modifications of Boron Nitride By Ion Implantation (Masters dissertation).
9. Sze, S.M., 2008. Semiconductor devices: physics and technology. John wiley & sons.
10. Kenari, M.F., 2019. Diffusion of implanted europium in glassy carbon. University of Pretoria (South Africa).
11. O'Connell, J.H., 2009. Characterization of hydrogen and helium implanted silicon carbide (Masters dissertation, Nelson Mandela Metropolitan University; Faculty of Science).

12. Nastasi, M., Mayer, J.W. and Hirvonen, J.K., 1996. Ion-solid interactions: fundamentals and applications. Cambridge University Press.
13. Gibbons, J.F., 1968. Ion implantation in semiconductors—Part I: Range distribution theory and experiments. Proceedings of the IEEE, 56(3), pp.295-319.
14. El-Kareh, B. and Hutter, L.N., 1995. Fundamentals of semiconductor processing technology. Springer Science & Business Media.
15. Ziegler, J.F., Ziegler, M.D. and Biersack, J.P., 2010. SRIM–The stopping and range of ions in matter (2010). Nuclear Instruments and Methods in Physics Research Section B: Beam Interactions with Materials and Atoms, 268(11-12), pp.1818-1823.
16. Stoller, R.E., Toloczko, M.B., Was, G.S., Certain, A.G., Dwaraknath, S. and Garner, F.A., 2013. On the use of SRIM for computing radiation damage exposure. Nuclear instruments and methods in physics research section B: beam interactions with materials and atoms, 310, pp.75-80.

Chapter 4 : Diffusion

Diffusion is the movement of ions along a concentration gradient. The atoms move from a region of high concentration to a region of low concentration. These atoms move from lattice site to lattice site. Two conditions must be satisfied for the atoms to move, firstly there must be an unoccupied adjacent site next to the atom. Secondly, the atom must have enough energy to break its bonds with neighboring atoms and slightly cause lattice distortion as it shifts position [1]. The rate of diffusion is influenced by several factors. Temperature plays an important role on the rate of diffusion. As the temperature rises, so does the rate of diffusion [1]. Additionally, the presence of defects in the material serves as a driving force for diffusion.

4.1 Diffusion mechanisms

4.1.1 Vacancy mechanism

The vacancy mechanism is the most common and dominant form of diffusion [2]. A perfect crystal is one with atoms in their correct lattice sites, however such a crystal does not exist. All crystalline solids contain vacancies. These vacancies serve as the primary means for diffusion. In thermal equilibrium, there exists a certain concentration of vacant sites. Equation 4.1 can be used to estimate the number of vacancies in equilibrium. It is evident from equation 4.1 that the number of vacancies increases as the temperature increases.

$$N_v = Nexp\left(-\frac{Q_v}{kT}\right) \tag{4.1}$$

Where N is the total number of atomic sites, Q_v is the vacancy formation energy, T is the absolute temperature in Kelvins and k is the Boltzmann's constant.

Atoms adjacent to vacancies move by jumping into these vacancies, this is illustrated in figure 4.1. Each atom moves through the crystal by exchanging positions with vacancies located nearest to it [2,3]. Notably, as atoms and vacancies exchange positions, the diffusion of atoms in one direction corresponds to the motion of vacancies in the opposite direction. The extent to which vacancy diffusion occurs is influenced by the concentration of vacancies present in the material [1].

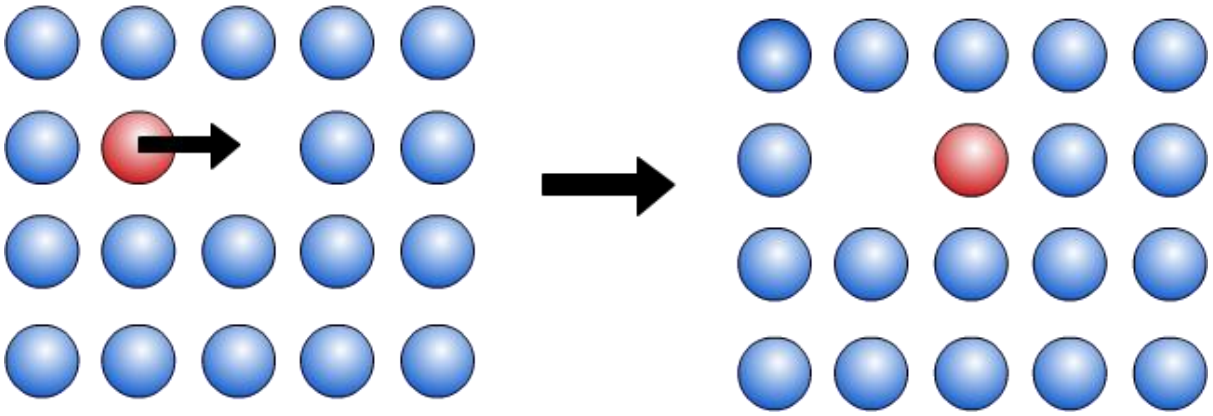

Figure 4.1: A representation of vacancy diffusion mechanism before and after an atom moves into a vacant site [4].

4.1.2 Interstitial and Interstitialcy Mechanism

In the interstitial diffusion mechanism, the diffusing atoms occupy the interstitial sites. This mechanism is illustrated in figure 4.2. The diffusing atoms are typically smaller than the host atoms and cause less lattice distortion [2,5]. Due to their small size, diffusing atoms exhibit higher mobility, and therefore interstitial diffusion occurs much faster than vacancy diffusion.

(a) (b)

Figure 4.2: A representation of interstitial diffusion mechanism, (a) before and after (b) interstitial diffusion [6].

Diffusion through the interstitialcy mechanism occurs when an interstitial atom is approximately the same size as the lattice atoms [7]. The interstitial atom pushes an atom in the lattice site into an interstitial site. The interstitial atom will then occupy the normal lattice site. Figure 4.3 illustrates the interstitialcy mechanism.

(a) (b)

Figure 4.3: An illustration of interstitialcy diffusion mechanism, (a) before and (b) after intersticialcy diffusion [6].

4.1.3 Diffusion by Grain boundaries and dislocations

Diffusion can also occur along dislocations and grain boundaries. Diffusion along dislocations and grain boundaries is typically referred to as short-circuit diffusion paths. This is because

atoms move faster along these paths. Grain boundaries are a type of interfacial defect. They separate regions with different crystal orientations in a material and are illustrated in figure 4.4.

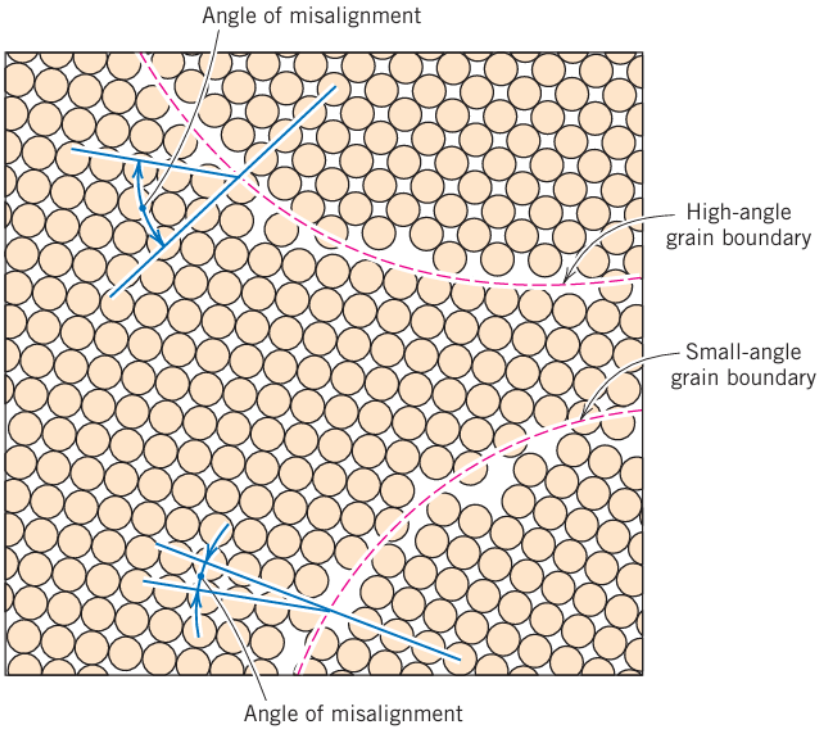

Figure 4.4: Schematic diagram showing grain boundaries [1].

Dislocations are one dimensional defects where atoms in a material are misaligned as shown in figure 4.5. Non-equilibrium processes like thermal processing and ion implantation result in dislocations. Unlike volume diffusion mechanisms, short-circuit diffusion paths do not require high temperatures to accelerate the rate of diffusion.

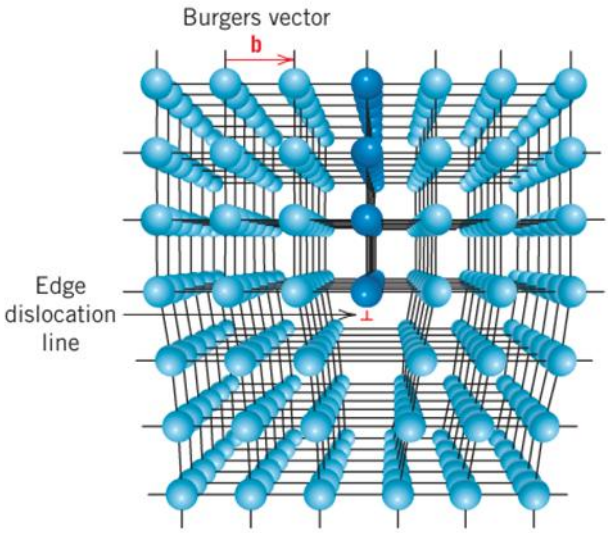

Figure 4.5: Schematic diagram of an edge dislocation [1].

4.2 Radiation Enhanced Diffusion

When a material is irradiated with energetic particles, atoms are displaced from the lattice and create vacancies and self-interstitials. Once these defects become mobile, they facilitate diffusion, leading to radiation-induced diffusion [7]. Radiation Enhanced Diffusion is a process in which a material is subjected to radiation, where the diffusion of atoms is significantly increased due to the presence of radiation-induced defects [8].

There are several forms of radiation enhanced diffusion, including segregation, reactive diffusion, oxidation enhanced diffusion, defect clustering and radiation enhanced surface diffusion.

1. Segregation: Impurity atoms diffuse within the host material but don't distribute evenly. Instead, they accumulate at specific locations within the host material [9].
2. Reactive diffusion: Two or more chemical species diffuse through a host material while simultaneously undergoing chemical reactions [10].

3. Oxidation enhanced diffusion: Oxidation introduces additional point defects in the lattice of the material. These defects facilitate the movement of impurity atoms, leading to enhanced diffusion [11].
4. Defect clustering: defects group together, creating regions of altered atomic structure that affect how atoms diffuse through the material. The clustering can enhance or hinder diffusion depending on the type and concentration of defects.
5. Radiation-Enhanced Surface diffusion: Radiation-induced defects, like vacancies and interstitials, increase the mobility of the surface atoms, leading to higher diffusion rates.

4.3 Fick's laws of diffusion and diffusion coefficients

The diffusion of atoms through a solid can be described by Fick's equations. The first equation relates the diffusion flux J to the gradient of concentration. The equation is called Fick's First Law, given by equation 4.2. This law gives information about the rate at which atoms diffuse.

$$J = -D\frac{dC}{dx} \tag{4.2}$$

Where D is the proportionality constant called the diffusion coefficient. The negative sign denotes the direction of diffusion down the concentration gradient. J is the flux, the concentration of atoms is given by C and $\frac{dC}{dx}$ indicate the concentration gradient [1,7].

In most practical diffusion cases, diffusion occurs under nonsteady state conditions, where both the diffusion flux and the concentration gradient change over time. Under these conditions, the

use of Fick's law becomes less practical to use and therefore the partial differential equation is used instead. This leads to Fick's second law given by equation 4.3 [1].

$$\frac{\partial C}{\partial t} = D\frac{\partial^2 C}{\partial x^2} \tag{4.3}$$

4.4 References

1. Callister, W.D. and Rethwisch, D.G., 2018. Materials science and engineering: an introduction. New York: Wiley.
2. Pelleg, J., 2016. Diffusion in ceramics (p. 448). Heidelberg: Springer.
3. Peterson, N.L., 1969. Diffusion in metals. Solid state physics, 22, pp.409-512.
4. University of Cambridge. (n.d.). Diffusion mechanisms. [online] Available at: https://www.doitpoms.ac.uk/tlplib/diffusion/diffusion_mechanism.php. (Accessed 18 February 2024)
5. Sze, S.M., 2008. Semiconductor devices: physics and technology. John wiley & sons.
6. Thabethe, T.T., 2017. The interfacial reaction and analysis of W thin film on 6H-SiC annealed in vacuum, hydrogen and argon. University of Pretoria (South Africa).
7. Mehrer, H., 2007. Diffusion in solids: fundamentals, methods, materials, diffusion-controlled processes (Vol. 155). Springer Science & Business Media.
8. Doyle, P.J., Benensky, K.M. and Zinkle, S.J., 2018. Modeling the impact of radiation-enhanced diffusion on implanted ion profiles. Journal of Nuclear Materials, 509, pp.168-180.
9. Allen, T.R. and Was, G.S., 2007. Radiation-enhanced diffusion and radiation-induced segregation. In Radiation Effects in Solids (pp. 123-151). Springer Netherlands.
10. Nicolis, G. and De Wit, A., 2007. Reaction-diffusion systems. Scholarpedia, 2(9), p.1475.
11. Antoniadis, D.A., Lin, A.M. and Dutton, R.W., 1978. Oxidation-enhanced diffusion of arsenic and phosphorus in near-intrinsic< 100> silicon. Applied Physics Letters, 33(12), pp.1030-1033.

Chapter 5 : Previous studies on ZrC

Numerous investigations have been conducted on zirconium carbide and its characteristics related to nuclear fuel applications [1,2,3,4]. These studies have advanced the understanding of the capabilities of ZrC. This chapter provides an overview of the research conducted on ZrC.

Xin *et al.* [5] investigated the effect of ZrC coating on graphite. The ZrC coatings were prepared by reactive melt infiltration. The surface morphologies of the samples were studied using SEM. XRD and EDS were used to study the crystalline structures and the elemental composition in the coating. The results showed that the phase composition of the coating was ZrC. The SEM images of the ZrC coating showed a smooth surface which was composed of crystals with hexagonal characteristics. Micro-cracks were present in the sample due to the rapid cooling from high temperature to room temperature after the coating process. A perfectly dense structure was observed. The compression strength of the sample was calculated. It was observed to increase from 30.8 to 35.0 MPa and it was compared to the graphite sample. The compression strength was found to have improved by 13.64%. This showed an improvement in the materials' strength and durability. The increase in compression strength for ZrC coated sample was attributed to the increase in density of ZrC.

Yang *et al.* [6] studied the microstructure and mechanical property changes induced by proton irradiation at a temperature of 800°C. The samples were irradiated with a beam of 2.8 MeV. Two irradiation doses of 0.7 dpa and 1.5 dpa were performed on the samples at 800°C. Microstructural changes were studied using SEM and TEM. The SEM images revealed that the annealed sample had low porosity, and the average grain size was found to be $\sim 24 \mu m$. After

irradiation, a thin oxidation layer formed on the surface. The TEM results showed that no voids were observed in the unirradiated and irradiated samples. No dislocation line or precipitates were formed. Frank loops were observed in the irradiated samples. The loops were observed to increase with an increase in irradiation dosage. XRD was performed to study lattice expansion of the samples. The data showed little peak shifts to a lower 2θ values with an increase in dose. The lattice parameters increased by approximately 0.09% at 0.7 dpa and 0.11% at 25 dpa. Microhardness and fracture hardness were studied. The microhardness was observed to increase as the irradiation dose increased. It had increased by 12.5% for 0.7 dpa and 14% for 1.5 dpa. The increase in hardening was explained to be due to the formation of point defects. Fracture hardness was observed to increase, for the sample irradiated at 1.5 dpa, the increase was about 79%.

Yang *et al.* [7] further investigated the effect of stoichiometry on the irradiation response of ZrC at temperatures relevant to HTGR. TEM was used to characterize the samples. It was observed that the irradiated ZrC had high density of dislocation loops. As the C/Zr ratio approaches stoichiometry, the dislocation loop density increased. Irradiation induced faceted voids were only observed in the $ZrC_{0.95}$ sample, which were attributed to the pre-existing dislocation lines. Graphite precipitates were also observed. Graphite precipitates were observed and were seen to be unfavorable as they can increase the size and density of dislocation loops in the ZrC. The C/Zr ratio was reported to have an effect on the irradiation response of ZrC and sub-stoichiometric ZrC improved irradiation resistance.

Wei *et al.* [8] investigated the effect of stoichiometry on the damage resistance and microstructure evolution of ZrC_x under irradiation with a 4 MeV gold ion beam. To conduct this study GIXRD and TEM were used to analyze the samples. It was observed that following

irradiation, the ZrC with different stoichiometries remained stable. Carbon vacancies present in the ZrC were seen to suppress the formation of dislocation loops which resulted in smaller dislocation loop sizes. ZrC_X with higher carbon vacancies were observed to have improved radiation damage tolerance.

Florez *et al.* [9] investigated the microstructural evolution of heavy ion irradiated ZrC at doses and temperature conditions relevant to the operation of high temperature reactors. The samples were prepared by hot pressing commercial ZrC powder. The samples were irradiated with 10 MeV gold ions at 800°C. Analysis of the samples was done using GIXRD, TEM and Raman spectroscopy. Increase in the irradiation dose resulted in the decrease in peak intensity and an increase in peak broadening. These changes were explained to be due to microstructural distortions and heterogenous microstrain. No amorphization was observed in the samples. Raman spectroscopy data revealed peaks associated with defects were intense and broader when radiation doses increased. These peaks were observed at Raman shifts of $\sim 204\ , \sim 275, \sim 515,\ and\ \sim 600\ cm^{-1}$.

Florez *et al.* [10] further investigated the early-stage oxidation of ZrC under ion irradiation and the effects of irradiation on the morphology and microstructure of the oxide formed on the surface of ZrC. GIXRD, electron microscopy (SEM and TEM) and Raman spectroscopy were used to characterize the samples. The results revealed that ZrC experienced early-stage oxidation leading to the formation of ZrO_2 precipitates on the surface. The morphology of the oxide was observed to have been influenced by the irradiation doses. Increase in irradiation dose resulted in the oxide precipitates becoming more faceted. The extent to which the surface of the ZrC was covered by oxide precipitates decreased with increasing irradiation doses. The

XRD data revealed the presence of the oxide phase in the near surface region and the ZrC peaks shifted to higher angles indicating dissolution of oxygen into the ZrC lattice.

Pellegrino *et al.* [11] investigated radiation effects in carbides: TiC and ZrC versus SiC. The aim was to provide insight into the use of carbides for nuclear fuel applications. Irradiation was conducted at room temperature with 1.2 MeV gold ions. Radiation damage was examined using RBS-C, XRD and Raman spectroscopy. The results revealed that TiC and ZrC maintain their crystalline structure at higher fluences while SiC readily becomes amorphized at lower fluences ($5x10^{13}$ – $1.7x10^{14}$ cm^{-2}). The ionicity of boning in TiC and ZrC contributed to their resistance against amorphization. The presence of structural flexibility in TiC and ZrC allows them to undergo structural changes without becoming amorphous. Their increased resistance to amorphization suggests their potential suitability for use in nuclear fuel applications. The different responses to irradiation were attributed to the fact that ZrC and TiC have a mixture of metallic, ionic, and covalent bonds while SiC has covalent bonds.

Pellegrino *et al.* [12] further conducted a Raman investigation of ion irradiated TiC and ZrC. The TiC and ZrC single crystals and polycrystals were implanted with 1.2 MeV gold ions at room temperature. The results showed that regardless of the fluence used, the optical and acoustic phonons were maintained, which indicated that there was no amorphization of both the ZrC and TiC samples. It was also observed that polycrystals were more tolerant to radiation than single crystals. As the fluence increased, a peak shift towards lower frequencies was noticed in the Raman spectra. This shift was linked to internal stress induced by irradiation. Additionally, the presence of defects, such as Frenkel pairs and dislocation loops, was observed.

Kim *et al.* [13] investigated the influence of high temperature annealing on the microstructure of ZrC. The annealing temperature was held at 1800°C and 1900°C. Analysis of the samples was carried out using TEM and Raman spectroscopy. The results showed that grain growth increased from approximately 0.4 μm to 3.2 μm with increasing annealing temperature. A reduction in the hardness of the samples was observed, it was seen to drop from approximately 29 to 24 GPa. The change in hardness was attributed to grain growth and tensile stress that was introduced into the material.

Biira *et al.* [14] investigated the thermal stability and properties of ZrC layers deposited by CVD. Deposition was carried out at 1400℃ for 2 hours. The samples were then annealed at various high temperatures. XRD, Raman spectroscopy and FE-SEM were used to characterize the samples. The results revealed that the crystallite size of ZrC layers increased as the annealing temperature increased. This was a sign of crystal growth in the samples. An increase in the lattice parameters as the annealing temperature increased was observed. The Raman data revealed that the samples contained free carbon. As the annealing temperature increased, the Raman peaks shifted and narrowed, which indicated a decrease in the amount of defects in the material. The hardness of the ZrC layers was observed to decrease with increasing annealing temperature. The surface morphology of the samples was observed to change with annealing temperature. As the annealing temperature increases from 1500℃ to 1800℃, the surface became less rough and voids between clustered particles closed resulting in a smoother surface. This was attributed to agglomeration and coalescence.

Craciun *et al.* [15] investigated the structural and mechanical changes induced in nanocrystalline ZrC thin films by Ar ion irradiation. The films were irradiated with 800 keV ions at room temperature and fluences of $1x10^{14}$,$1x10^{15}$, and $2x10^{15}$ cm^{-2}. The samples were

analyzed using GIXRD, AFM, SEM, and high-resolution TEM. It was seen that after irradiation the grain size increased greatly. The micro strain fluctuated; it went from 1.1 to 0.9 then 1.1 %. The lattice parameters were observed to increase. Irradiation led to a decrease in the density of the film. The crystallite sizes increased following irradiation which suggested a certain movement of atoms during irradiation. It was observed that fluences of $1x10^{14}$ cm^{-2} and $1x10^{15}$ cm^{-2} greatly reduced the nanohardness and Young's modulus. The films remained hard and elastic despite the decrease in hardness. Irradiation with the highest fluence of $2x10^{15}$ cm^{-2} did not cause any measurable decrease in the mechanical properties of the films.

Bao *et al.* [16] investigated the structural evolution in ZrC-SiC composites under high energy irradiation. Irradiation was conducted with 4 MeV Au^{2+} ions at a fluence of $5x10^{16}$ cm^{-2} at room temperature. The characterization techniques used were GIXRD, SEM and TEM. The damage region of SiC was found to be deeper ($\sim 1.55 \mu m$) than that of ZrC ($\sim 1.22\ \mu m$). Amorphization of SiC was seen and was followed by volume expansion. ZrC remained crystalline, however a large number of carbon vacancies formed under irradiation. The amorphization of SiC introduced compressive stress and led to a 0.49% decrease in the lattice parameters of ZrC. Grain boundaries were observed and acted as barriers which prevented the formation of cracks. The ZrC-SiC composite did not experience significant damage after being subjected to irradiation. This indicated that the sample was able to retain its structural integrity.

Azziz *et al*. [17] investigated the neutronic properties of ZrC of advanced TRISO fuel for high temperature gas cooled reactors. The study examined the effects of using ZrC in the coated fuel operating at different temperatures and levels of enrichment in the fuel. The Standard Reactor Analysis Code (SRAC) which is a computational tool for reactor physics analysis was used in this investigation. It was found that the use of ZrC increased the parasitic neutron capture in

the fuel system, resulting in lower core reactivity. Lower reactivity in the core was significant at lower enrichments of uranium fuel of 11.25 and 15%. The reactivity loss gradually diminished at high temperatures (1500K). This revealed the importance of the design value of uranium enrichment. A slight hardening in the neutron spectrum was observed, this was attributed to parasitic neutron absorption by Zr atoms. The study revealed that as the fuel temperature increased, the multiplication factor also increased, indicating inherent safety of the core. These results revealed that ZrC demonstrated favorable behaviour for a reactor design.

Mardiyanto *et al.* [18] investigated the penetration depth of Silver (Ag) and Palladium (Pd) fission products in the ZrC layer using SRIM/TRIM simulation. The simulation was carried out for energies between 0.10-5.00 MeV for both Ag and Pd, extending up to 10.00 MeV exclusively for Pd. The results showed that the penetration depth increased with increasing ion kinetic energy. The penetration depth of Pd in ZrC at the highest energy (10 MeV) was found to be 19.500Å and was 11.500Å for Ag at an energy of 5 MeV. The study showed that there is a clear relationship between the kinetic energy of the ions and penetration depth.

To the best of my knowledge no work has been done on the impact of europium fission product on the microstructure of ZrC. Given that Eu is one of the fission products that are released from the TRISO particle, it is important to examine how Eu could potentially influence the structural integrity of ZrC.

5.2 References

1. Katoh, Y., Vasudevamurthy, G., Nozawa, T. and Snead, L.L., 2013. Properties of zirconium carbide for nuclear fuel applications. Journal of Nuclear Materials, 441(1-3), pp.718-742.
2. Harrison, R.W. and Lee, W.E., 2016. Processing and properties of ZrC, ZrN and ZrCN ceramics: a review. Advances in Applied Ceramics, 115(5), pp.294-307.
3. Minato, K., Ogawa, T., Sawa, K., Ishikawa, A., Tomita, T., Iida, S. and Sekino, H., 2000. Irradiation experiment on ZrC-coated fuel particles for high-temperature gas-cooled reactors. Nuclear Technology, 130(3), pp.272-281
4. Snead, L.L., Katoh, Y. and Kondo, S., 2010. Effects of fast neutron irradiation on zirconium carbide. Journal of nuclear materials, 399(2-3), pp.200-207.
5. Xin, Y., Zhe-an, S., Qi-zhong, H., Li-yuan, C., Ping, Z. and Liang, X. (2014). A zirconium carbide coating on graphite prepared by reactive melt infiltration. Journal of Central South University, (21), pp.472–476.
6. Yang, Y., Dickerson, C.A., Swoboda, H., Miller, B. and Allen, T.R., 2008. Microstructure and mechanical properties of proton irradiated zirconium carbide. Journal of Nuclear Materials, 378(3), pp.341-348.
7. Yang, Y., Lo, W.Y., Dickerson, C. and Allen, T.R., 2014. Stoichiometry effect on the irradiation response in the microstructure of zirconium carbides. Journal of Nuclear Materials, 454(1-3), pp.130-135
8. Wei, B., Wang, D., Wang, Y. and Zhang, H., 2019. Microstructure Evolution in ZrC x with Different Stoichiometries Irradiated by Four MeV Au Ions. Materials, 12(22), p.3768.

9. Florez, R., Crespillo, M.L., He, X., White, T.A., Hilmas, G., Fahrenholtz, W. and Graham, J., 2020. The irradiation response of ZrC ceramics under 10 MeV Au3+ ion irradiation at 800 ºC. Journal of the European Ceramic Society, 40(5), pp.1791-1800.
10. Florez, R., Crespillo, M.L., He, X., White, T.A., Hilmas, G., Fahrenholtz, W.G. and Graham, J., 2020. Early stage oxidation of ZrC under 10 MeV Au3+ ion-irradiation at 800° C. Corrosion Science, 169, p.108609.
11. Pellegrino, S., Thomé, L., Debelle, A., Miro, S. and Trocellier, P., 2014. Radiation effects in carbides: TiC and ZrC versus SiC. Nuclear Instruments and Methods in Physics Research Section B: Beam Interactions with Materials and Atoms, 327, pp.103-107.
12. Pellegrino, S., Trocellier, P., Thomé, L., Miro, S., Costantini, J.M. and Jouanny, E., 2019. Raman investigation of ion irradiated TiC and ZrC. Nuclear Instruments and Methods in Physics Research Section B: Beam Interactions with Materials and Atoms, 454, pp.61-67.
13. Kim, D., Chun, Y.B., Ko, M.J., Lee, H.G., Cho, M.S., Park, J.Y. and Kim, W.J., 2016. Microstructure evolution of a ZrC coating layer in TRISO particles during high-temperature annealing. Journal of Nuclear Materials, 479, pp.93-99.
14. Biira, S., Thabethe, T.T., Hlatshwayo, T.T., Bissett, H., Ntsoane, T. and Malherbe, J.B., 2020. Investigating the thermal stability of the chemical vapour deposited zirconium carbide layers. Journal of Alloys and Compounds, 834, p.155003.
15. Craciun, D., Socol, G., Simeone, D., Behdad, S., Boesl, B., Vasile, B.S. and Craciun, V., 2016. Structural and mechanical properties changes induced in nanocrystalline ZrC thin films by Ar ion irradiation. Journal of Nuclear Materials, 468, pp.78-83.

16. Bao, W., Liu, J.X., Wang, X., Zhang, H.B., Xue, J., Sun, S.K., Xu, F., Xue, J. and Zhang, G.J., 2018. Structural evolution in ZrC-SiC composite irradiated by 4 MeV Au ions. Nuclear Instruments and Methods in Physics Research Section B: Beam Interactions with Materials and Atoms, 434, pp.23-28.
17. Aziz, F., Panitra, M., Rivai, A.K., Silalahi, M., Sabrina, N., Dani, M., Setiawan, M.B. and Setiadipura, T., 2020. Investigation on neutronic properties of ZrC coated advanced TRISO fuel for high-temperature gas-cooled reactors. In Journal of Physics: Conference Series (Vol. 1436, No. 1, p. 012036). IOP Publishing.
18. Mardiyanto, M., Shabrina, N. and Rivai, A.K., 2023. Investigation of Ag and Pd fission products penetration depth in ZrC layer of HTGR TRISO fuel particle using SRIM/TRIM monte carlo simulation. Jurnal Sains dan Teknologi Nuklir Indonesia (Indonesian Journal of Nuclear Science and Technology), 24(2), pp.59-65.

Chapter 6 : Experimental Procedure

In this study, the effects of europium (Eu) ion implantation and subsequent annealing on the microstructure of zirconium carbide (ZrC) were investigated, along with the diffusion behaviour of europium. Spark plasma sintering (SPS) was used to prepare the ZrC samples. The ZrC substrates were then implanted with Eu ions a fluence of 1×10^{16} cm^{-2} and subsequently annealed in hydrogen gas for 2 hours at 600℃, 700℃ and 800℃. The resulting microstructural changes induced by ion implantation and annealing were investigated using Scanning electron microscopy (SEM). The elemental composition was determined using Energy dispersive spectroscopy (EDS). X-ray diffraction (XRD) was used for phase identification, to analyze strain, lattice structure and determine the crystal size. Rutherford backscattering spectrometry (RBS) was used to study the diffusion behaviour of europium (Eu).

6.1 Sample Preparation.

In this study, ZrC substrates were prepared by spark plasma sintering (SPS) process. Sintering is the process of firing and solidifying powders at temperatures below their melting point. During this process, the particles bond together and eliminate the voids, resulting in dense structures [1,2]. SPS is a direct current, low-voltage, pulse current-activated pressure method. External pressure and an electric field are employed concurrently during sintering to improve the densification of the powder compacts [1]. SPS is performed in four major stages. The first stage involves the removal of gases and the creation of a vacuum. Then, in the second stage, pressure is applied, followed by resistance heating in the third stage, and lastly, cooling in the fourth stage [3].

The zirconium carbide powder of mean particle size 5 nm and purity >99 % from Sigma-Aldrich was used. An electronic mass balance was used to weigh the ZrC powder, ensuring that equal amounts of ZrC powder were used for the spark plasma sintering (SPS) process. A graphite die with an inner diameter of 20 mm was used to make the powders. A 0.2 mm thick graphite foil was placed between the die and powder for easy removal and to ensure that the cooling of the sintered ZrC samples was uniform. To reduce radiation loss, the outside of the graphite die was covered with an insulating felt. After placing the powder in the graphite die, it was cold pressed with a hydraulic press to consolidate the powder together before being spark plasma sintered (SPS). The ZrC ceramic pellets were sintered using the HHPD-25 from FCT Syteme GmbH Germany at Tshwane University of Technology. The SPS process was carried out in vacuum (0.05 bar) at a temperature of 2100 °C at a heating rate of 100 °C/min until the desired temperature was reached. Sintering required a holding time of 10 minutes and a pressure of 50 MPa. The samples were rapidly cooled to room temperature at the end of the sintering cycle.

After that, the samples were cut into smaller pieces with a diamond saw and polished with a Saphir 550 SemiAutomatic Grinder/Polisher. The samples had a diameter of 20 mm and a thickness of about 5 mm. After, the ZrC samples were cleaned four times using an ultrasonic bath with acetone for 3 to 4 minutes to remove any particles on the surface. After that, it was washed with MA 02 soap. It was then repeatedly rinsed with deionized water. Methanol was also used four times to remove excess water from the sample before being blown away by nitrogen gas.

Implantation was performed in the Institute für Festkörperphysik, Friedrich-Schiller-Universität, Jena, Germany. Figure 6.1 presents an illustration of the ion beam setup for all

accelerators and beam lines. The europium ions (Eu) were implanted with a fluence of $1\times10^{16}cm^{-2}$ at the energy of 360 keV into ZrC at room temperature (RT). The flux was maintained at a rate below 10^{13} cm^{-2} s^{-1} to avoid beam induced target heating of the sample. The incident angle was set to be 7° with respect to the normal incident, to avoid channeling from taking place during implantation. The process of sample preparation and analysis is illustrated in figure 6.2.

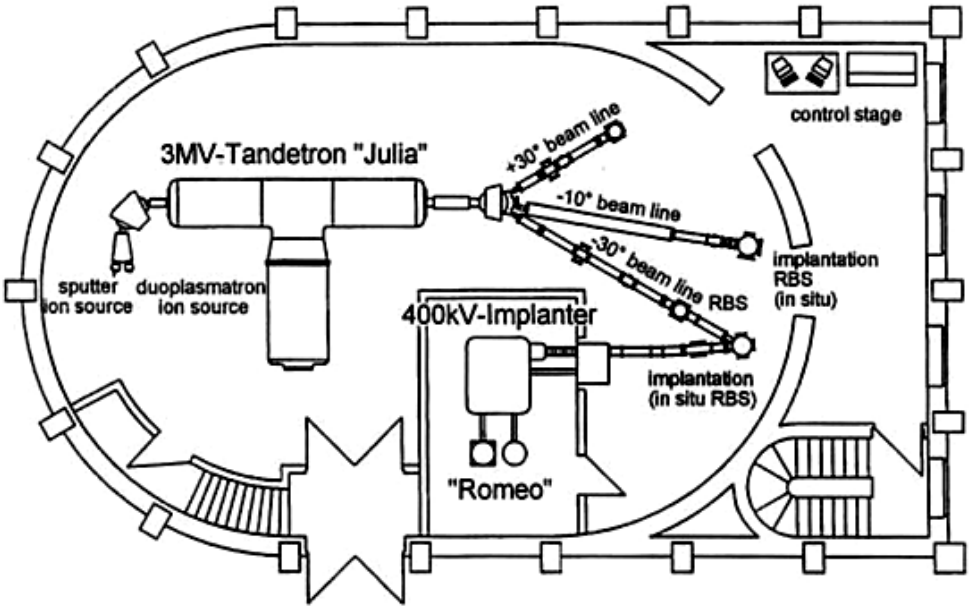

Figure 6.1: Illustration of the Ion Beam Laboratory at the Institute of Solid-State Physics, Friedrich-Schiller-Universität Jena, Jena, Germany [4].

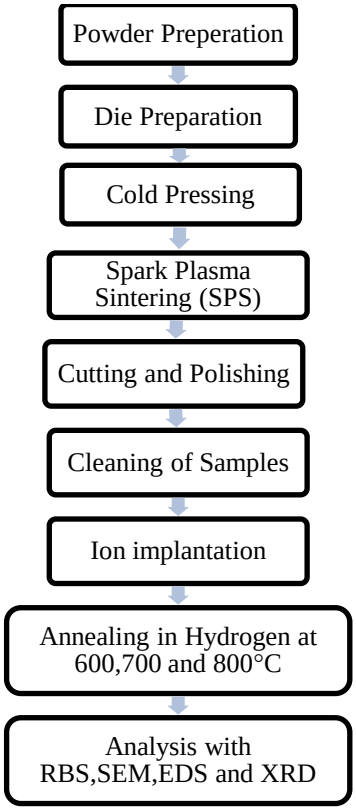

Figure 6.2: A schematic diagram of the sample preparation and analysis techniques used in this study.

6.1.1 Annealing

The implanted samples were annealed in hydrogen gas at temperatures of 600℃, 700℃ and 800℃ for 2 hours at a heating rate of 10°/min. Elevated temperatures influence the crystal structure, facilitating damage recovery caused by ion implantation and thus improving the crystallinity of the material. The samples were then placed in a glass tube which was connected to a flow meter of different gas supplies. In this study H_2 99.99 % purity was used. The flow rate of H_2 was 250 SCCM. After annealing, the oven was left to cool before taking the sample out.

ZrC is widely used in nuclear applications, particularly as a coating material in HTGRs and TRISO coated fuel particles. Exposure to hydrogen-rich environments in nuclear reactors can

introduce strain into the material, potentially affecting its structural integrity. Since ZrC is prone to oxidation, hydrogen was chosen as it acts as a strong reducing agent, preventing unwanted oxidation during the annealing process. Additionally, hydrogen helps maintain a controlled atmosphere in the annealing furnace, minimizing contamination from reactive gases such as oxygen.

Annealing in H_2 was conducted to simulate the temperature and gas environment in the reactor. In nuclear reactors, hydrogen interacts with coated fuel particles, which can impact the performance and longevity of the coating layers. The diffusion of hydrogen into ZrC may induce structural changes and alter thermal properties, potentially leading to embrittlement or structural failure. Understanding these interactions is crucial for enhancing ZrC's effectiveness as a protective barrier in nuclear fuel systems.

6.2 Analysis Techniques

6.2.1 Scanning Electron Microscopy (SEM)

To analyze the surface morphology before and after implantation, SEM was used. In the SEM, a focused beam of electrons scans the sample and creates a detailed image that reveals the structure of the sample. SEM is capable of much higher resolution and magnification (>100,000X), allowing it to see much smaller objects at the atomic level [5,6]. There are several qualitative characteristics of a sample that can be obtained from SEM, including its topography, morphology, crystallography, composition, etc. [7].

6.2.1.1 Typical Scanning Electron Microscopy Instrumentation

A typical SEM has the following components: an electron gun (electron source and accelerating anode), electromagnetic lenses for focus, a vacuum chamber, a sample stage, and a variety of detectors for collecting signal emitted by the sample as depicted in figure 6.3 [8].

The electron gun, located at the highest point of the scanning electron microscope, generates a steady supply of electrons with modifiable energy [9]. There are currently three types of electron guns in use: tungsten and lanthanum hexaboride thermionic electron guns, as well as the field emission gun [10]. The field emission gun (FEG) was used for this investigation. A single crystal tungsten wire with a very sharp tip is used to create an electron source in the FEG [11]. The SEM electron optical setup includes electromagnetic lenses (including the condenser and objective lens), apertures, stigmator, and scan coils. As a result of these elements coming together, a precise electron beam is created that rasters over the desired area of the sample. The electron beam is scanned across the sample's surface, point by point, from left to right [12].

The pump system and vacuum chamber make up the vacuum system. A rough pump and a turbo molecular pump create the vacuum. The vacuum prevents the electron beam from interacting with gas atoms in the SEM system [13]. During SEM operation, the sample chamber is located at the bottom of the electron column and is kept under vacuum. The sample is placed on a holder/stub in a sample stage [8-12]. The signals generated by beam interaction with the sample are processed by detectors which convert it into an electronic signal that is then displayed as a digital image. The most common signal collected are secondary electrons by secondary electron detector (Everhart–Thornley), backscattered electrons by solid-state

detectors (Solid-State detectors), and X-ray signals by energy dispersive spectrometer (EDS) detectors [5].

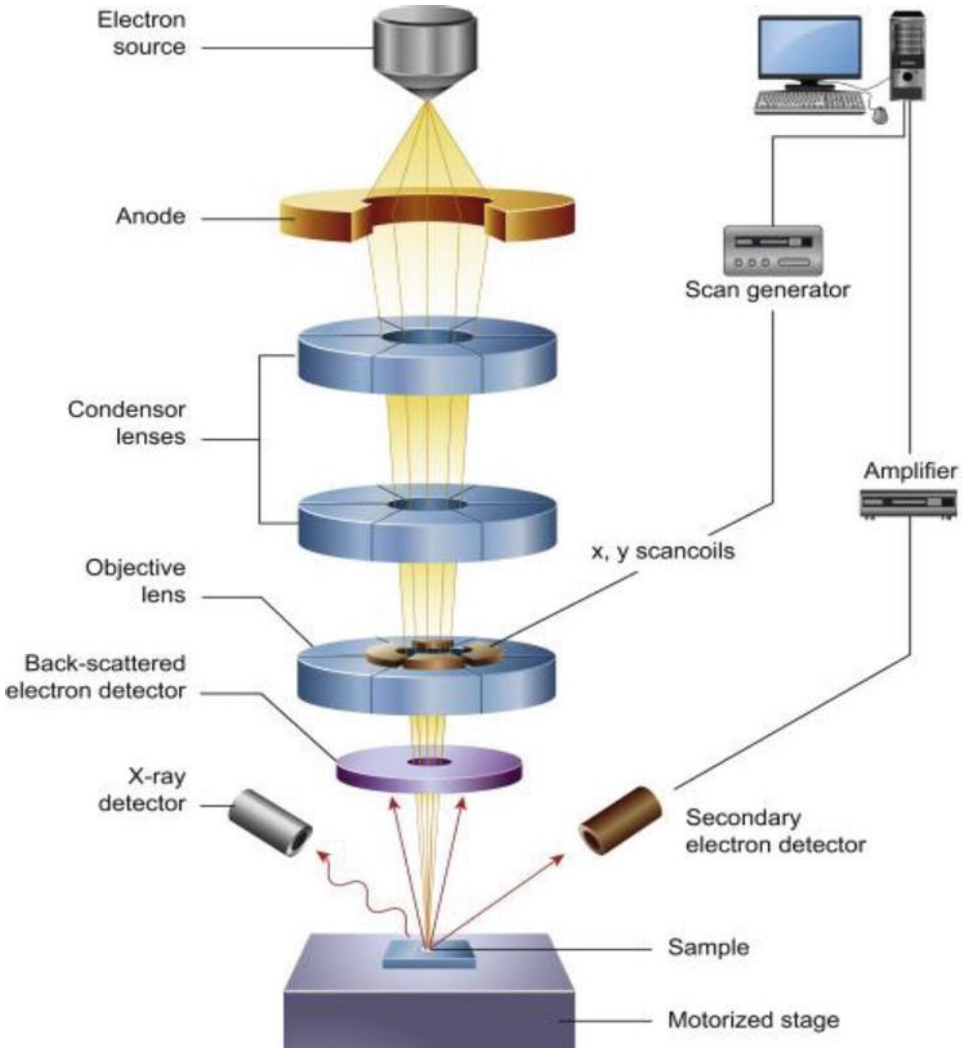

Figure 6.3: Representation of a typical SEM showing key components [9].

6.2.1.2 Interaction of electron beam with the sample

During interaction of the electron beam with the sample, an electron beam is produced by the electron gun. The electron beam travels through a vacuum column, passing through electromagnetic fields and lenses that focus and direct it towards the sample for high resolution imaging. A deflection coil mechanism guides the beam in a raster pattern across the surface of

the sample. Figure 6.4 depicts the result of an incident beam on a sample, producing Secondary electrons (SE), auger electrons, back scattered electrons (BSE), Characteristic X-rays, and cathodoluminescence. Electrical detectors capture the emitted signals, which are then converted into digital images and displayed on a screen [5].

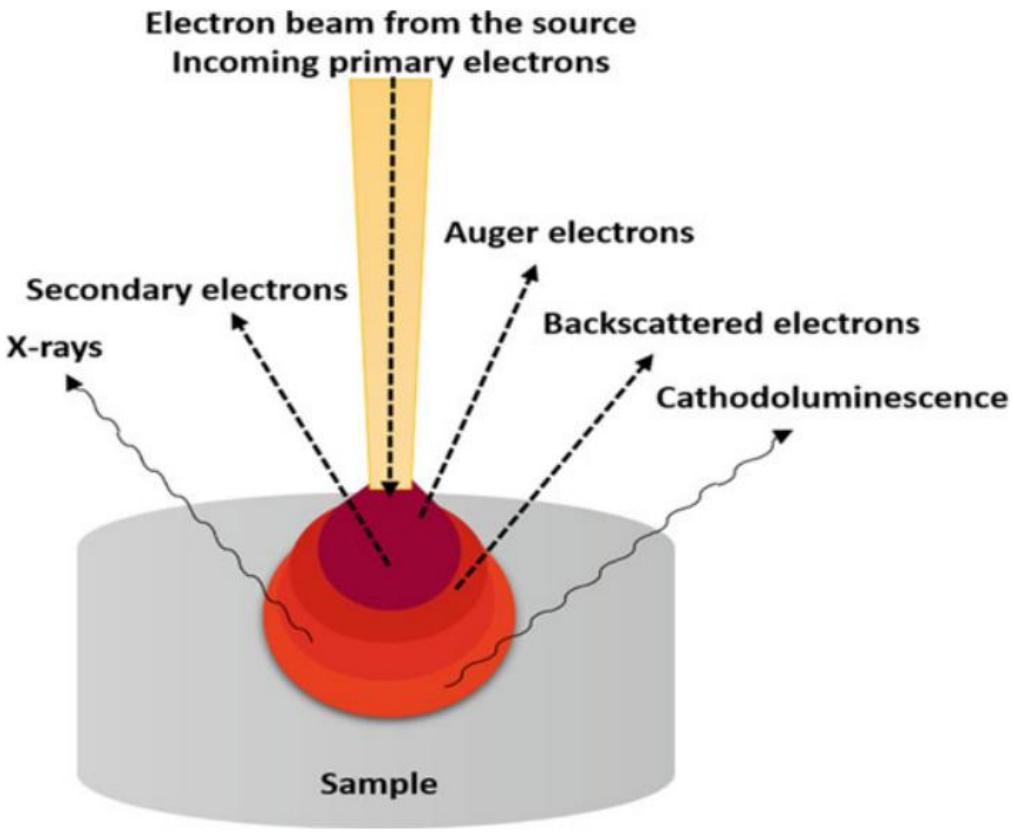

Figure 6.4: Interaction of electron beam with sample and emitted signals [7].

In scanning electron microscopy, the primary signals used to form images are backscattered and secondary electrons [9]. When the primary beam strikes the sample surface, ionizing the sample atoms, loosely bound electrons are emitted, which are known as secondary electrons. They can only escape from a region within a few nanometers of the material surface due to their low energy, which is typically around 3-5 eV. As a result, secondary electrons precisely

mark the position of the beam and provide high-resolution topographic data. Surface structures can be resolved down to the order of 10 nm using a secondary electron signal [5,11].

Backscattered electrons are incident electrons that come close enough to an atom's nucleus to be deflected at a larger angle and then re-emerge from the surface. They have much higher energies [14]. These are used to distinguish areas of different elements present in the sample. Elements with a higher atomic number give off more backscattered electrons and appear brighter than those with a lower number. Crystallographic information can also be obtained from backscattered electrons [5,14]. Characteristic x-rays are another type of signal produced by the interaction of the primary electron beam with the sample. The most commonly used microanalytical technique in the SEM is the analysis of characteristic x-rays to provide chemical information [11].

In this study, the Zeiss Ultra 55 Field Emission SEM (FE-SEM) from University of Pretoria was used to analyze the surface morphology of the ZrC samples. The microscope was operated in in-lens mode, with beam energies of 1 KeV.

6.2.2 Energy Dispersive X-ray Spectroscopy (EDS)

To characterize the elemental composition of the ZrC samples before and after implantation, EDS was used. Energy Dispersive X-Ray Spectroscopy (EDS) is a chemical microanalysis technique used in together with scanning electron microscopy (SEM) [6]. EDS can detect elements with atomic numbers greater than boron, and these elements can be detected at concentrations of at least 0.1%. Material evaluation and identification, contamination

identification, spot detection analysis of regions up to 10 cm in diameter, quality control screening, and other applications are all possible with EDX [15].

This technique uses incident beam electrons to produce X-rays within the atoms of the sample [16]. The primary beam enters the sample and interacts with its inner shell. As a result, electrons from the target atoms' inner shells are ejected from their orbits. When an electron is ejected from an atom, the atom is left with a vacancy in its electron orbital. This causes the atom to be in an ionized state [12]. The vacancy will be filled by an electron transition whereby an electron from a higher shell fall back to fill in the gap. Because this electron has a higher energy than the original electron, it releases energy in the form of an x-ray [16] as shown in figure 6.5.

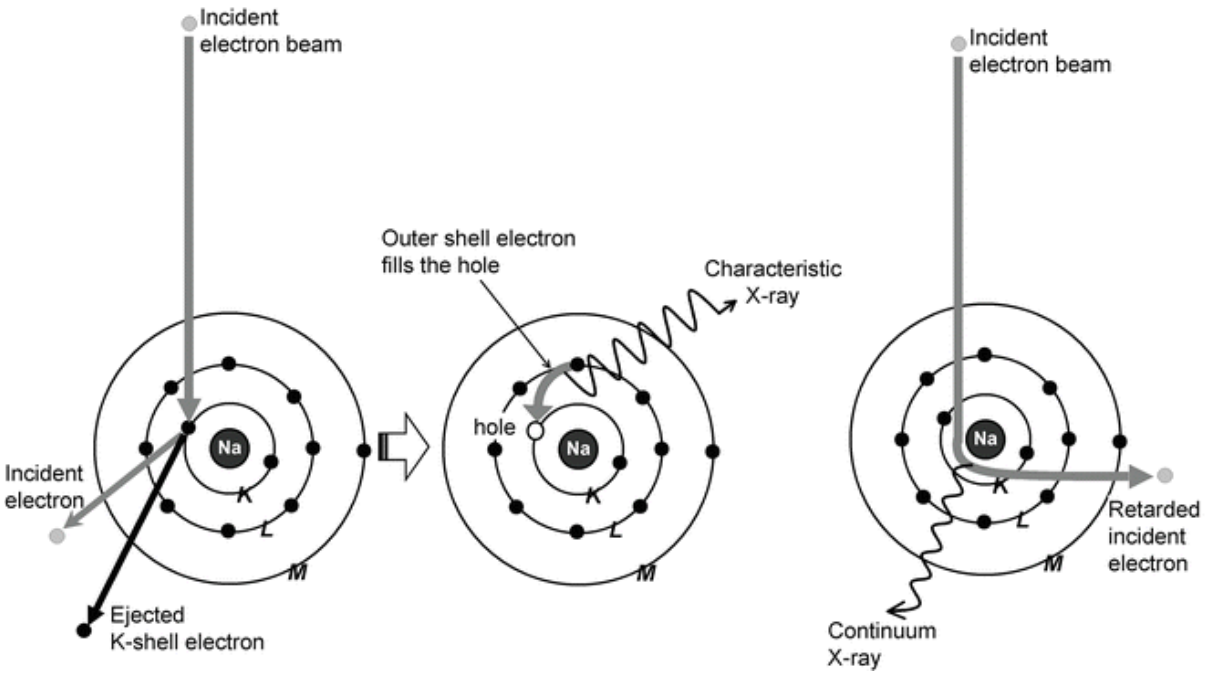

Figure 6.5: A representation of the generation of characteristic X-rays from a sample by an incident electron beam [16].

Each element has a distinct atomic configuration that results in a distinct set of peaks on an X-ray radiation spectrum [17]. Each atom has electron shells that exist around its nucleus. The atomic energy level is the amount of energy that each shell around the atom has. It represents a specific element's characteristic energy. As a result, the difference in the energy levels of these electron shells is regarded as an element's characteristic value. As such, electron transitions between any two shells result in the emission of X-ray photons with energies specific to each element. These X-ray photons have distinct energy values and occupy distinct positions in the x-ray spectrum [12].

The EDS X-ray detector quantifies the abundance of emitted x-rays in relation to their energy. When an X-ray strikes the detector, it generates a signal based on the energy of the X-ray. A charge-sensitive preamplifier converts this signal to a voltage pulse. The signal is then sent to a multichannel analyzer, which categorizes the signals by voltage. The energy determined by the voltage measurement is sent to a computer for display and further data analysis for each incident X-ray. By examining the spectrum of X-ray energy and counts, the elemental composition of the sample can be identified [6].

In this study, the EDS instrument which is used in conjunction with the FE-SEM from the university of Pretoria was used to characterize the elemental composition of ZrC. The operation voltage of 10 KeV was used to collect the EDS spectra.

6.2.3 X-ray Diffraction (XRD).

X-ray diffraction (XRD) is a highly effective nondestructive method for characterizing crystalline and amorphous materials. Materials to be characterized can be in the form powders, thin films, coatings and solids.

X-rays are electromagnetic radiation with energies ranging from about 200 eV to 1 MeV [18]. They lie between the ultraviolet light and gamma rays in the electromagnetic spectrum. Their high energy allows them to penetrate opaque materials. Sources of X-rays include synchrotron and conventional laboratory X-ray tubes. The latter uses sealed tubes and rotating anodes to produce X-rays. During this process, electrons are generated by heating a tungsten filament cathode which is maintained at a high negative potential. The X-rays are produced by directing a high-voltage electron beam toward a metal anode inside a vacuum-sealed X-ray tube as shown in figure 6.6.

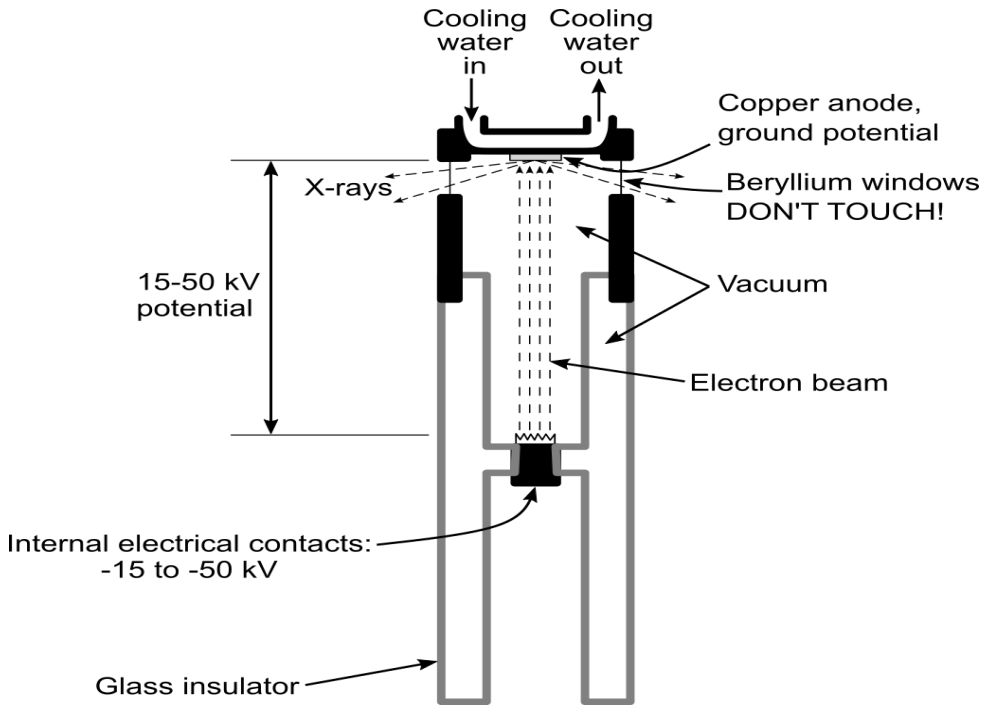

Figure 6.6: Diagram of an X-ray where X-rays are produced [19].

These electrons are accelerated toward the anode, typically held at ground potential. The high velocity electrons collide with the water-cooled anode and lose energy. Their energy loss during the impact produces white radiation [18,20]. When an incident electron has enough energy to eject an inner-shell electron, the atom becomes excited and creates a vacancy in its electron shell. When an electron from a higher shell fills this void, an X-ray photon with energy equal to the difference in electron energy levels is produced. The X-ray photon's energy is specific to the target [18]. Characteristic X-ray spectra are produced when electrons have enough energy to dislodge inner shell electrons of the target material. These spectra are made up of several components, the most common of which are K_α and K_β. K_α is made up, in part, of $K_{\alpha1}$ and $K_{\alpha2}$. $K_{\alpha1}$ has a slightly shorter wavelength than $K_{\alpha2}$ and twice the intensity. The wavelengths are specific to the target material (Cu). To generate monochromatic X-rays for diffraction, filtering with foils or crystal monochromator is required. $K_{\alpha1}$ and $K_{\alpha2}$ have similar wavelengths, so the average of the two is used. CuK_α radiation with a wavelength of 1.5418 Å is the most common target material for single-crystal diffraction.

The fundamental principle of X-ray diffraction is the constructive interference of X-rays scattered from a crystalline sample [21]. When the incident rays of a fixed wavelength get scattered from the sample at certain incident angles, they lead to constructive interference (and a diffracted ray) if Braggs law is satisfied [21]. When this constructive interference occurs, a diffracted beam of X-rays will leave the crystal at an angle equal to that of the incident beam. Figure 6.7 gives an illustration of this observation. The position of the diffracted peak is given by Bragg's law, equation 6.1 which relates the wavelength (λ) of the probing X-ray beam, the spacing between the atomic planes (d), and the angle of diffraction (θ) [22].

$$2dsin\theta = n\lambda \tag{6.1}$$

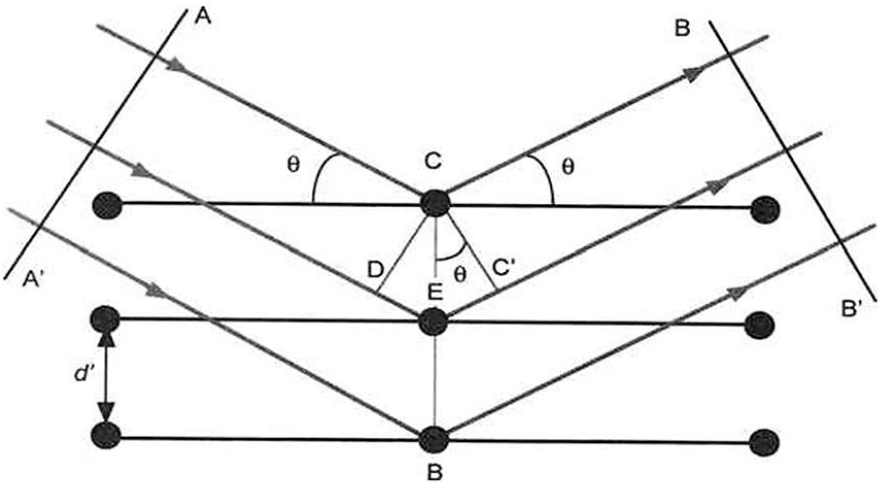

Figure 6.7: Illustration of the diffraction of an incident beam (Bragg's law) [20]

XRD provides valuable insights into different aspects of materials, including crystal structure and size, phase identification, crystallographic orientation, lattice parameter determination, dislocation density, residual stress or strain, and phase transformations [20] as depicted in figure 6.8.

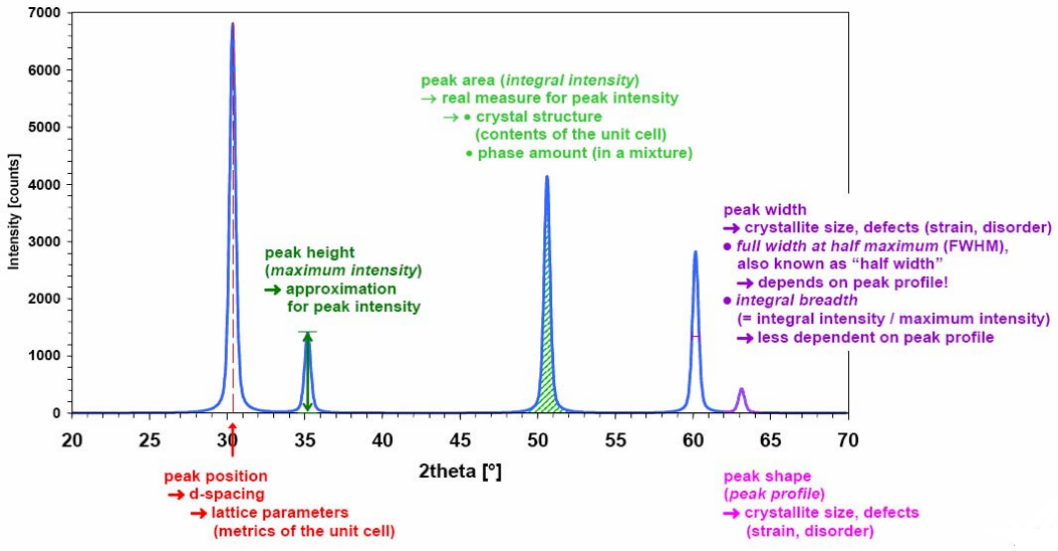

Figure 6.8: A typical XRD pattern and the type of information that can be extracted [21].

6.2.3.2 Phase Identification

The use of XRD is a convenient and reliable technique for identifying materials by determining their crystal structure and comparing them with the standard diffraction patterns on the International Centre for Diffraction Data (ICDD) [21]. X-ray diffraction patterns are unique to each crystalline solid and are like fingerprints [22]. An examination of the diffraction pattern is required to identify phases present in a material. This includes peak positions, intensities, widths and background shape [23]. Identify three peaks that appear most intensely on the diffraction pattern. The positions (2θ) of these peaks should correspond to the positions of reflections for a known phase in a database, such as ICCD. These reflections should be in similar order as those found in the database [21,24].

6.2.3.3 Crystal Size

The average crystallite size in materials can be determined using XRD. The principle behind determining crystallite or grain size is that a decrease in crystallite size leads to an increase in diffraction width (peak broadening). Debye Scherrer developed equation 6.2 to estimate particle size [25]:

$$D = \frac{K\lambda}{\beta cos\theta} \tag{6.2}$$

where D is the crystallite size, K is the Scherrer constant (0.9), θ is the angle of diffraction, λ is the wavelength of the X-ray used and β is the full width at half maximum (FWHM).

When calculating the crystal size, it is important to take note of peak broadening (β) of XRD peaks which arise from instrumental effects, crystallite size and lattice strain [20]. To obtain accurate crystallite size estimates, instrumental broadening must be subtracted before applying the Scherrer equation. The corrected broadening is obtained using equation 6.3 [26].

$$\beta = \sqrt{\beta_{obs}^2 - \beta_i^2} \tag{6.3}$$

Where β is the corrected FWHM used in the Scherrer equation. β_{obs} is the measured FWHM of the diffraction peak and β_i is the instrumental broadening

The Scherrer constant is a dimensionless shape factor which estimates the crystal size from the broadening of XRD peaks. The value of K varies depending on the shape and structure of the crystal. K has been determined to vary between 0.62 and 2.08 and is commonly taken as 0.89 [27].

6.2.3.4 XRD experimental setup

In general, an XRD setup is made up of these main components: An X-ray source, primary optics for beam shaping, sizing and condition; sample stage, and secondary optics, filter to remove K_β contamination as well as an X-ray detector for detection of scattered beam.

In this study, XRD analysis was conducted at the South African Nuclear Energy Corporation (NECSA) X-ray diffraction facility. A Bruker D8 Advance diffractometer shown in figure 6.9 was used to analyze the samples. Qualitative identification of the chemical phases was done using the Search/Match technique where the measured diffraction peaks (intensities and peak

positions) are matched against the known patterns from International Centre for Diffraction Data (ICDD) PDF-4+ 2023 database entries using the sieve+ software. Software data processing of the as-measured diffraction patterns in preparation for the Search/Match procedure comprised subtracting a baseline background and stripping the $K_{\alpha 2}$ X-ray beam contamination.

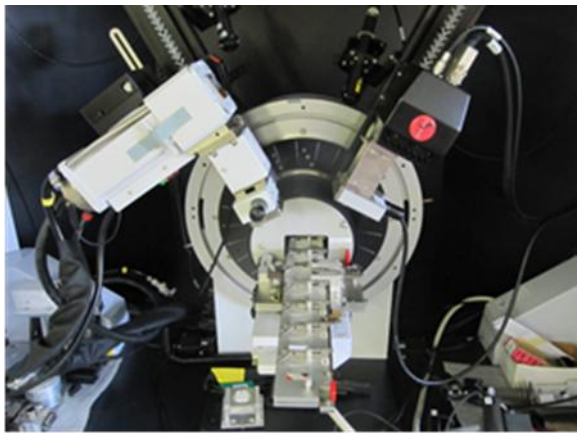

Figure 6.9: A photograph of the D8 Advance diffractometer used for the analysis.

The beam irradiated the sample at an incident angle of 5°, and measurements were collected over a 2θ range from 20° to 90°. Diffraction data was recorded using a Lynx Eye position-sensitive detector. The measurements were performed according to the instrument setup and experimental parameters summarized in Table 6.1.

Table 6.1: Instrument set up and experimental parameters used for analysis.

Description	Parameter
Diffractometer	D8 Advance
Goniometer	θ-θ
Target tube	Cu-radiation
Scan type	Detector scan
Wavelength	1.5406Å
2θ range	20˚ to 90˚
Step size	0.02˚
Count time/step	4.0 seconds
Sample stage	Flip-stick-sample changer stage
Sample holder	Standard open disk sample holder
Primary optics	Goebel mirror
	6 mm exit slit
	Cu absorber
	0.6 mm anti-divergent slit
	2.5˚ Soeller
Secondary Optics	Lyn Iris
	Anti-scattered chamber
	Ni filter
	2.5˚ Soeller
Detector	PSD Lynx eye

6.2.4 Rutherford Backscattering Spectrometry (RBS)

Rutherford backscattering spectrometry (RBS) is a quantitative, nondestructive technique for the elemental analysis, thickness, and depth profiles of solids in the near surface region [28,29]. It is possible to determine the elemental composition of the target sample by analyzing the energy distribution of scattered ions (energy spectrum) [30]. Using RBS spectrums, we can obtain valuable quantitative information about the distribution of elements at the surface of a

substrate. There are several types of information included in this, such as information about the mass and composition of the scattering atoms [29].

It is based on the collision of atomic nuclei. A beam of monoenergetic ions, usually H^+ or He^+ (alpha particles), with energies ranging from 0.5 to 3 MeV, is directed at the sample. These high energy ion beams are bombarded and penetrate into the sample and backscattered ions are examined carefully to determine their energy distributions and yields at specific angles [29,31]. During this process, elastic Coulomb scattering occurs between the projectile and the target nuclei. Some ions may backscatter from the sample after colliding with the target atoms. Backscattered ions have different energies depending on the mass of the target atom. By measuring the energy spectrum of these backscattered ions, RBS can provide detailed information about the composition of the surface region extending to a depth of several micrometers [32].

6.2.4.1 Kinematic Factor

During RBS, ions are back-scattered elastically when an incident ion of mass M_1 and atomic number Z_1 strike a target nuclei with mass M_2 and atomic number Z_2. The energy of the scattered ions (E) is determined by the mass of the target nucleus (M_2) and the scattering angle. This is based on the principles of conservation of momentum and energy (see equation 6.4) [29,30].

$$\frac{E_1}{E_0} = K = \left[\frac{(M_2^2 - M_1^2 sin^2\theta)^{1/2} + M_1 \cos\theta}{M_1 + M_2}\right]^2 \quad (6.4)$$

where $\frac{E_1}{E_0}$ is the energy ratio called the kinematic factor. M_1 and M_2 are the masses of the incident ion and target atom, respectively. The scattering angle is denoted by θ.

6.2.4.2 Differential cross section

Electrostatic repulsion is observed when the incident particle and the target nucleus interact. The incident particle penetrates the sample and collides with the target nuclei at shallow depths. The incident particles also interact with the electrons in the sample. These interactions result in the energy loss of the incident particles. This action allows for the use of RBS in determining the depth profile and thickness of layers in the sample. This is due to the fact that particles which backscatter from the surface of the sample have significantly more energy than the particles that backscatter within the sample's depth. It is important to note that both the charge Z of the target and incident nuclei is critical for determining the scattering cross section (probability of detection) [28,32]. The differential cross section is given by equation 6.5 [33].

$$\frac{d\sigma}{d\Omega} = \left(\frac{Z_1 Z_2 e^2}{4E}\right)^2 \times \frac{4\left(\sqrt{1-\left(\left({}^{M_1}/_{M_2}\right)\sin\theta\right)^2}+\cos\theta\right)^2}{(\sin\theta)^4\sqrt{1-\left(\left({}^{M_1}/_{M_2}\right)\sin\theta\right)^2}} \tag{6.5}$$

where Z_1 and Z_2 are the atomic numbers of the incident ion and target atom respectively. E is the energy of the incident ion and e is the electronic charge. From equation 6.4 it is seen that the scattering cross section is essentially proportional to the square of the atomic number of the target atom. This indicates that RBS is more sensitive to heavier elements as opposed to lighter elements [33].

6.2.4.3 Instrumentation and Working

Figure 6.10 illustrate a typical RBS set-up. Particle accelerators are used to generate ion beams in standard RBS equipment. Van de Graaff and Cockcroft and Walton accelerators are the two most commonly used types of accelerators for producing MeV ion beams. These accelerators use a magnet to analyze and select the desired ion energy while removing unwanted ion species. After passing through the analyzing magnet, the ions are focused to a size of about 1 mm through small openings called apertures. Then, the ion beam is directed into a scattering chamber, where the sample targets are mounted on a manipulator. A target current or a beam monitor system is typically installed between the final aperture and the target area to monitor the beam current. This helps in monitoring the number of ions in the beam. The detection of backscattered ions is usually performed using a solid - state detector which is installed inside the chamber to measure the energy spectrum of backscattered ions. The signals from the detector are amplified and assorted in energy in a multichannel analyzer [29,31].

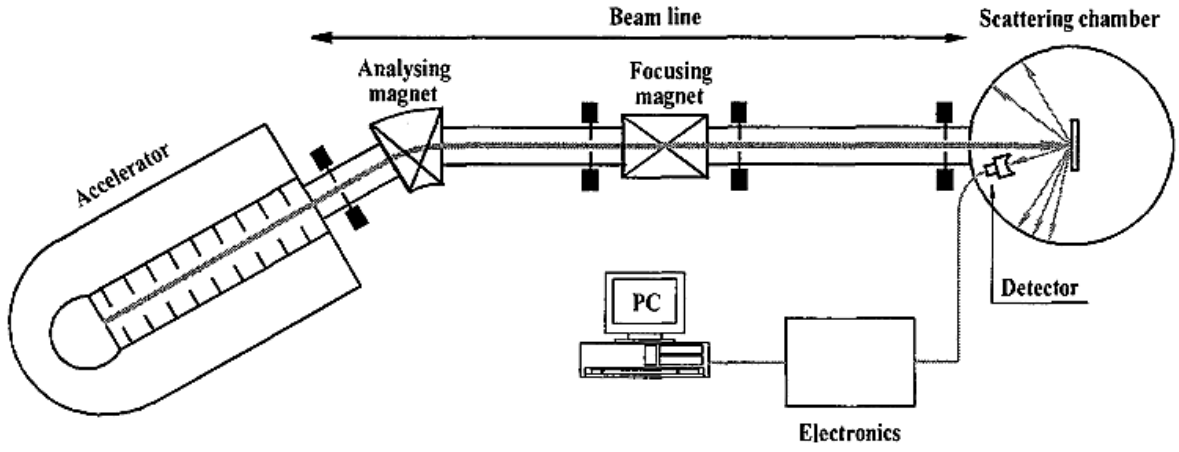

Figure 6.10: Schematic overview of the RBS set-up [32].

The 3MV Tandetron accelerator from iThemba LABS was used in this study. Helium ions (He^{+}) were accelerated to an energy of 2 MeV. The experiment was carried out with a charge

of 20 μC and beam current at 45 nA while a scattering angle of 165˚ was used for measurements.

6.3 References

1. Cavaliere, P. ed., 2019. Spark plasma sintering of materials: advances in processing and applications. Springer.
2. Viswanathan, V., Laha, T., Balani, K., Agarwal, A. and Seal, S., 2006. Challenges and advances in nanocomposite processing techniques. Materials Science and Engineering: R: Reports, 54(5-6), pp.121-285.
3. Saheb, N., Iqbal, Z., Khalil, A., Hakeem, A.S., Al Aqeeli, N., Laoui, T., Al-Qutub, A. and Kirchner, R., 2012. Spark plasma sintering of metals and metal matrix nanocomposites: a review. Journal of Nanomaterials, 2012, pp.18-18.
4. http://www.physik2.uni-jena.de/inst/exphys/ionen/accessed July 2014.
5. Kannan, M., 2018. Scanning electron microscopy: Principle, components and applications. A Textbook on Fundamentals and Applications of Nanotechnology; Springer: Berlin/Heidelberg, Germany, pp.81-92.
6. . Hanke, L.D., 2001. Handbook of analytical methods for materials. Materials Evaluation and Engineering Inc., Plymouth, pp.35-38
7. Akhtar, K., Khan, S.A., Khan, S.B. and Asiri, A.M., 2018. Scanning electron microscopy: Principle and applications in nanomaterials characterization. Handbook of materials characterization, pp.113-145.
8. Hübschen, G., Altpeter, I., Tschuncky, R. and Herrmann, H.G. eds., 2016. Materials characterization using nondestructive evaluation (NDE) methods. Woodhead publishing.
9. Goldstein, J.I., Newbury, D.E., Echlin, P., Joy, D.C., Lyman, C.E., Lifshin, E., Sawyer, L. and Michael, J.R., 2003. Scanning Electron Microscopy and X-ray Microanalysis. Boston, MA: Springer US.

10. Kaufmann, E.N., 2003. Characterization of Materials, 2 Volume Set. Wiley-Interscience.
11. Zhou, W., Apkarian, R., Wang, Z.L. and Joy, D., 2007. Fundamentals of scanning electron microscopy (SEM). Scanning Microscopy for Nanotechnology: Techniques and Applications, pp.1-40.
12. Ul-Hamid, A., 2018. A beginners' guide to scanning electron microscopy (Vol. 1, p. 402). Cham, Switzerland: Springer International Publishing.
13. Schmitt, R., 2014. Scanning Electron Microscope. In: Laperrière, L., Reinhart, G. (eds) CIRP Encyclopedia of Production Engineering. Springer, Berlin, Heidelberg.
14. Vernon-Parry, K.D., 2000. Scanning electron microscopy: an introduction. III-Vs Review, 13(4), pp.40-44.
15. Abd Mutalib, M., Rahman, M.A., Othman, M.H.D., Ismail, A.F. and Jaafar, J., 2017. Scanning electron microscopy (SEM) and energy-dispersive X-ray (EDX) spectroscopy. In Membrane characterization (pp. 161-179). Elsevier.
16. Kuo, J. ed., 2008. Electron microscopy: methods and protocols (Vol. 369). Springer Science & Business Media.
17. Mishra, R.K., Zachariah, A.K. and Thomas, S., 2017. Energy-dispersive X-ray spectroscopy techniques for nanomaterial. In Microscopy methods in nanomaterials characterization (pp. 383-405). Elsevier.
18. Bunaciu, A.A., UdriŞTioiu, E.G. and Aboul-Enein, H.Y., 2015. X-ray diffraction: instrumentation and applications. Critical reviews in analytical chemistry, 45(4), pp.289-299.

19. Philips Xrd: X-ray tube. (n.d) Kurt Hollocher. Available at: https://muse.union.edu/hollochk/the-x-ray-tube/ (Accessed: 13 December 2024).
20. Suryanarayana, C., Norton, M.G., Suryanarayana, C. and Norton, M.G., 1998. X-rays and Diffraction (pp. 3-19). Springer US.
21. Epp, J., 2016. X-ray diffraction (XRD) techniques for materials characterization. In Materials characterization using nondestructive evaluation (NDE) methods (pp. 81-124). Woodhead Publishing.
22. Sharma, R., Bisen, D.P., Shukla, U. and Sharma, B.G., 2012. X-ray diffraction: a powerful method of characterizing nanomaterials. Recent research in science and technology, 4(8).
23. Ermrich, M. and Opper, D., 2013. XRD for the Analyst: Getting Acquainted with the Principles. PANalytical.
24. Skorbun, A.D., Gabielkov, S.V. and Zhyganiuk, I.V., 2021. Method for Identifying Crystalline Phases in X-ray Diffraction Data from Multiphase Samples. arXiv preprint arXiv:2108.07176.
25. Ameh, E.S., 2019. A review of basic crystallography and x-ray diffraction applications. The international journal of advanced manufacturing technology, 105, pp.3289-3302.
26. Waseda, Y., Matsubara, E. and Shinoda, K., 2011. X-ray diffraction crystallography: introduction, examples and solved problems. Springer Science & Business Media.
27. Kurapati, S. and Srivastava, P.K., 2018. Application of Debye-Scherrer Formula in the determination of Silver nano particles shape. International Journal of Management, Technology And Engineering, 8(81).

28. Herman, M.H., 1984. Applications of Rutherford backscattering spectrometry to refractory metal silicide characterization. Journal of Vacuum Science & Technology B: Microelectronics Processing and Phenomena, 2(4), pp.748-755.
29. Palmetshofer, L., 2011. Rutherford backscattering spectroscopy (RBS). Surface and Thin Film Analysis, pp.191-202.
30. Chirayil, C.J., Abraham, J., Mishra, R.K., George, S.C. and Thomas, S., 2017. Instrumental techniques for the characterization of nanoparticles. In Thermal and rheological measurement techniques for nanomaterials characterization (pp. 1-36). Elsevier.
31. Kimura, K., 2006. Rutherford Backscattering Spectroscopy. Encyclopedia of Analytical Chemistry: Applications, Theory and Instrumentation.
32. INTERNATIONAL ATOMIC ENERGY AGENCY., 2000. Instrumentation for PIXE and RBS, IAEA-TECDOC-1190, IAEA, Vienna.
33. Baumann, S.M., 1992. Rutherford backscattering spectrometry. Encyclopedia of Materials Characterization, Surfaces, Interfaces, Thin Films, Butterworth-Heinemann, Boston, MA, pp.476-487.

Chapter 7 : Results and Discussion

This study examines the impact of europium ion implantation and subsequent annealing on the microstructure of zirconium carbide (ZrC), as well as the diffusion behavior of europium. The ZrC samples were subjected to europium ion implantation at a fluence of $1x10^{16}$ cm^{-2} at room temperature, using an energy of 360 KeV. The implanted samples were then annealed from 600℃ to 800℃ for 2 hours in hydrogen gas. Hydrogen gas, combined with elevated temperature was used to simulate nuclear reactor conditions. This approach enabled the study of annealing and hydrogen exposure effects on the structural changes of the Eu-ZrC sample. After annealing at each temperature, the samples were characterized using Scanning Electron Microscopy (SEM), Energy Dispersive Spectroscopy (EDS), X-ray Diffraction (XRD) and Rutherford Backscattering Spectrometry (RBS). This chapter presents and discusses the findings.

7.1 SRIM simulation and Rutherford Backscattering Spectrometry (RBS)

The Stopping and Range of Ion in Matter (SRIM) simulation program was used to model the implanted ion behaviour in ZrC during ion implantation. Figure 7.1 shows the simulated results. The penetration depth of Eu was found to be 67 nm indicating that the ions were implanted relatively close to the surface. The relative atomic density (RAD) at this depth was found to be approximately 2%, which suggests that is the maximum concentration of Eu ions at 67 nm. The maximum radiation damage obtained using SRIM was 2 dpa with a damage profile at a depth of 40 nm, which is much closer to the surface. This indicates that most ZrC atoms were displaced near the surface.

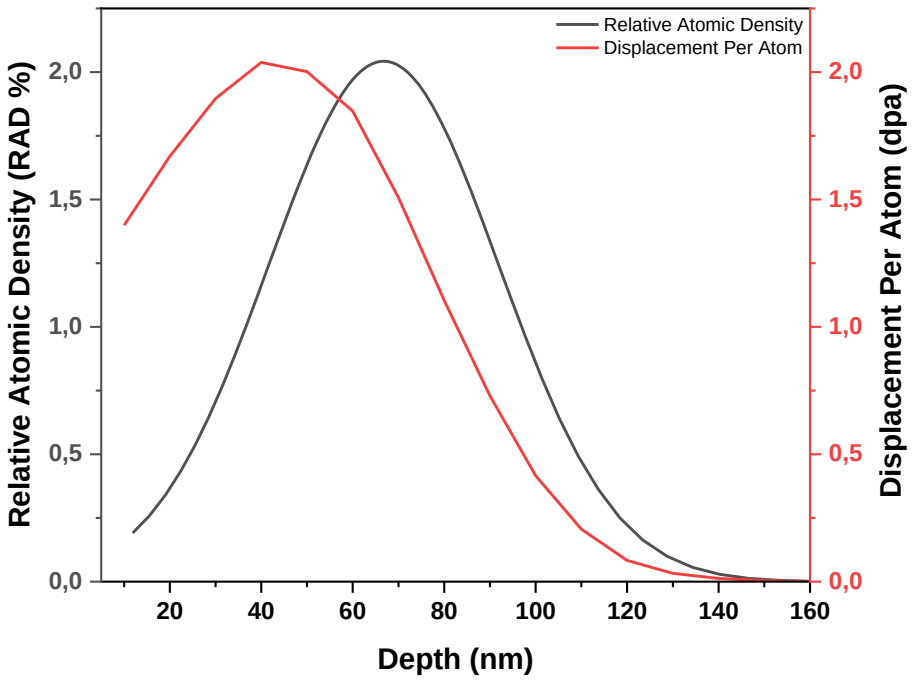

Figure 7.1: Depth profile of Eu ions and displacement per atom obtained from SRIM simulation.

RBS was performed to verify the implantation of Eu in ZrC, determine its location within the material, and analyze its behavior following annealing. Figure 7.2 shows a comparison of the Eu depth profiles for the as-implanted sample and the SRIM simulation. The maximum energy of the RBS system used was not enough to completely resolve Eu from ZrC. The experimental data of the as-implanted sample showed a projected range of Eu ions approximately 76 nm from the surface, while SRIM simulated a projected range of 67 nm, resulting in a 9 nm discrepancy between the simulated and experimental results. This could be due to the limitations of the SRIM program. SRIM focuses only on direct collisions between the incident ion and the target, and it does not take into account the structural changes and reorganization that happen during ion implantation. The program does not account for recombination of knocked off atoms with vacancies in the crystal lattice.

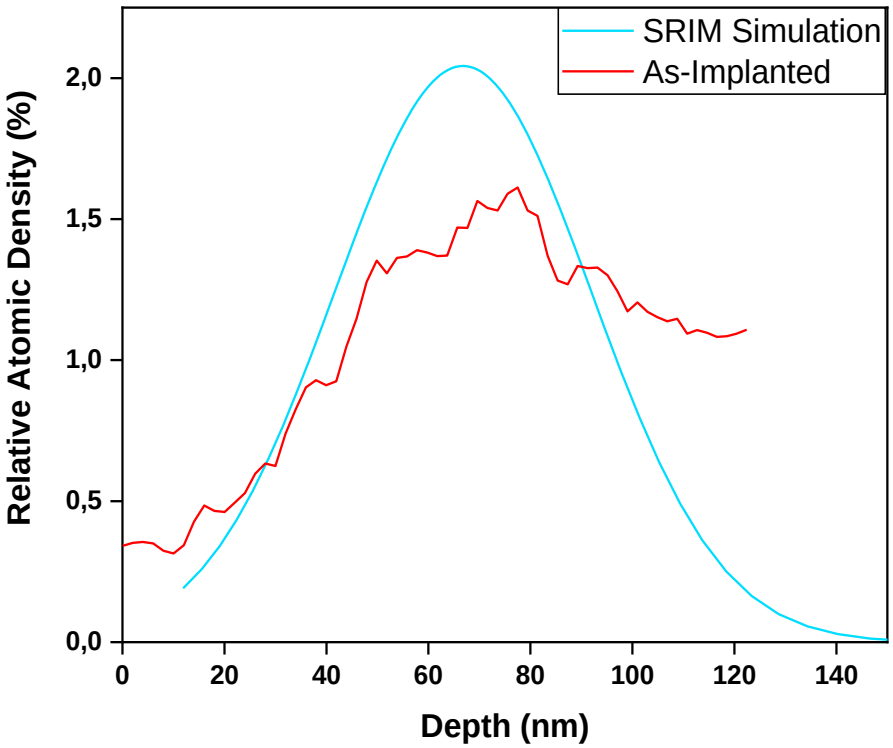

Figure 7.2: Depth profile of europium from SRIM simulation and the As-Implanted RBS data.

Figure 7.3 shows the RBS spectra of the as-implanted sample, and the samples annealed at 700℃ and 800℃. From the RBS spectra C, Zr and Eu surface positions were detected at channel numbers of 201, 833 and 898 respectively. This information was extracted using the spectral management software (SPEKVERW).

The RBS spectra of the as-implanted sample shows that indeed europium was present in the sample, indicating successful implantation. Annealing at 700℃ resulted in the europium ions being spread out and shifting towards the surface. This could be due to migration of europium towards the ZrC substrate surface. At 800℃ there was little to no Eu ions left in the ZrC substrate.

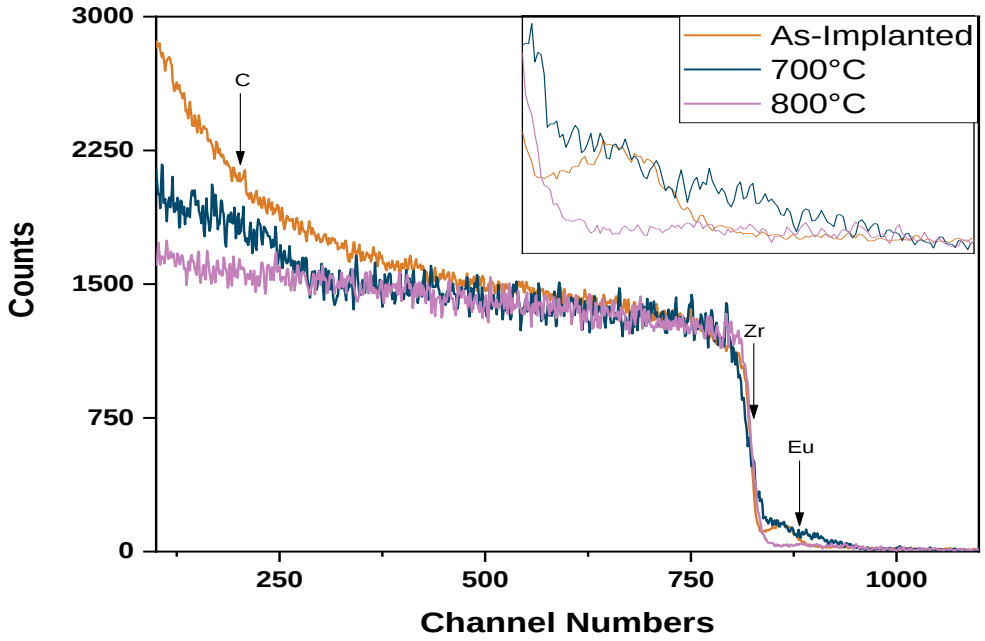

Figure 7.3: RBS spectra of the As-Implanted, 700℃ and 800℃ annealed samples.

7.2 Scanning Electron Microscopy (SEM)

To study the near surface morphology of the samples, SEM was used. Magnification of 20KX and an energy of 1 keV was used to take the SEM images. Figure 7.4 shows the SEM images of the virgin, implanted and Eu-ZrC sample annealed from 600℃ to 800℃. The virgin sample was observed to have some cracks and small unevenly distributed grains. After ion implantation, the surface appeared smoother with polishing marks, however some cracks remained present. Annealing at 600℃ resulted in an uneven surface, the high points and edges appear brighter while the flat areas appear to be darker. Small closely packed clusters of grains with different sizes were observed.

After annealing at 700℃ bigger crystals were observed and appeared to push against each other. This resulted in smaller voids in the sample. Annealing at 800℃ resulted in a surface that is more irregular than observed previously. The difference in the surface evolution of the ZrC samples may be attributed to the reactivity of Eu. In a hydrogen environment, Eu can react with hydrogen to form europium hydride (EuH_2). Eu also reacts with oxygen to form europium oxide ($2Eu_2O_3$). Additionally, Eu combusts at temperatures between 150℃ - 180℃ in the presence of oxygen, which could contribute to a rougher surface appearance. These reactions followed by combustion of Eu could have contributed to the surface deteriorating. Hollow cracks and voids were observed. The observed cracks could be attributed to the cooling process following annealing. These cracks and voids could have served as pathways for Eu to move further to the surface, hence a shift in the europium peak is observed in the RBS spectra.

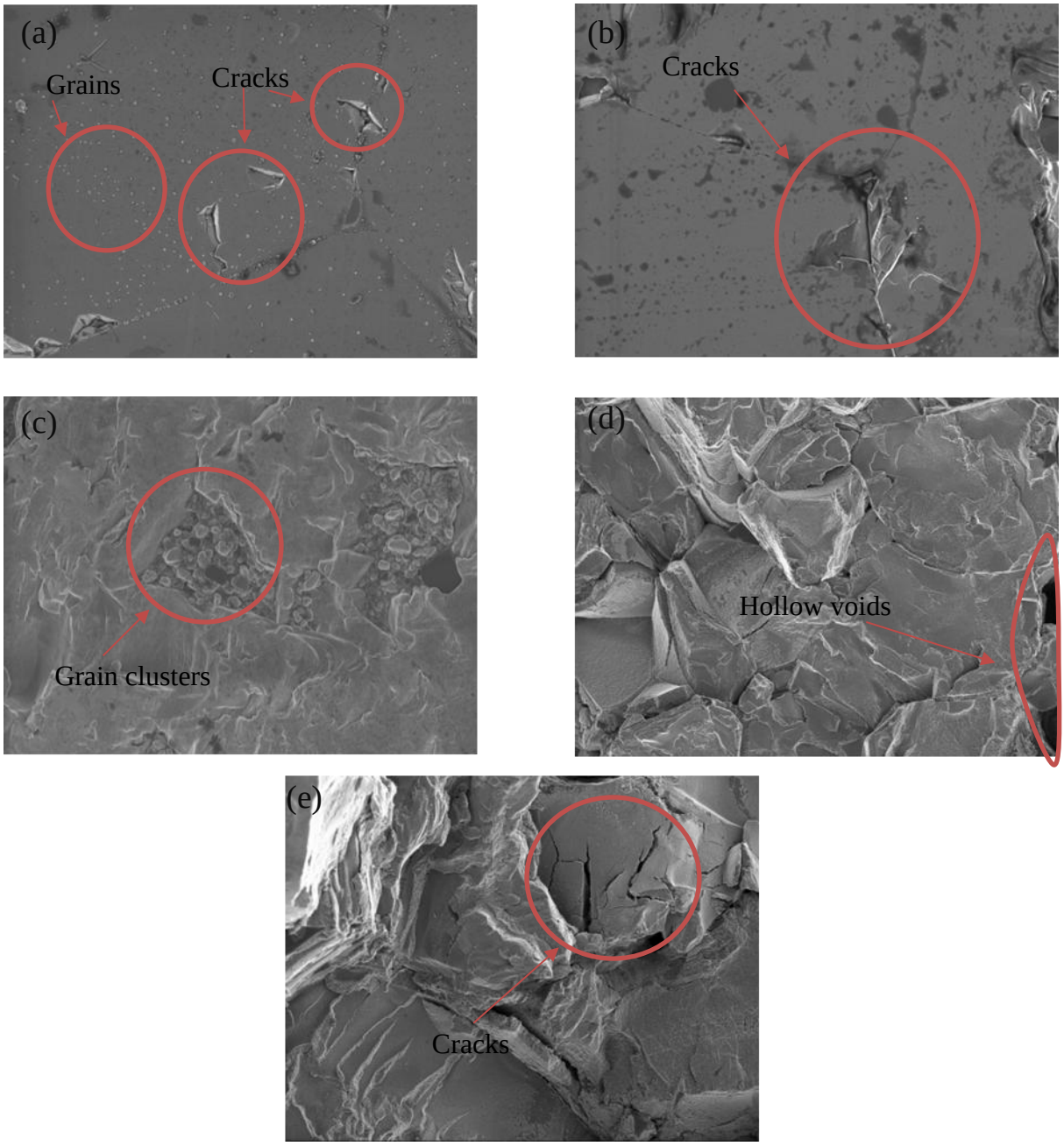

Figure 7.4: SEM images of ZrC sample (a) before implantation, (b) after implantation with Eu ion at a fluence of 1x10^{16} cm^{-2} at RT; annealed at (c) 600℃, (d) 700℃ and (e) 800℃.

7.3 Energy Dispersive X-ray Spectroscopy

EDS was conducted to obtain the elemental composition of ZrC after implantation and annealing at various temperatures. The goal was to confirm the presence of europium in the sample. The results in table 7.1 show the obtained elements.

EDS elemental analysis of the as-implanted detected small traces of titanium (Ti), approximately 0.28 wt%, which likely originated from the equipment used during the sample synthesis or handling. Traces of europium (Eu) were also observed at about 0.69 wt%, confirming the success of the implantation process and indicating that europium ions were effectively incorporated into the ZrC matrix. Other detected elements included zirconium (Zr) at approximately 61.60 wt%, and oxygen (O) at about 4.48 wt%. The observed oxygen presence can be attributed to the inherent tendency of ZrC to readily oxidize upon exposure to air, leading to the formation of a thin zirconium oxide (ZrO_2) layer on the surface. Haung *et al* [1] observed formation of stable ZrO_2 after annealing from 600℃ to 1000℃. After annealing at 700℃, a significant increase in the europium content was observed, rising from 0.69 to 1.81 wt%. This suggests that europium migrated towards the surface, likely due to enhanced diffusion at elevated temperatures, as supported by the RBS measurements, which showed a deeper presence of europium closer to the surface after annealing.

Additionally, a notable increase in oxygen content from 4.48 to 19.34 wt% was recorded. This could be due to a reaction between zirconium and oxygen during annealing, forming a thick ZrO_2 layer on the surface. Although annealing in a hydrogen atmosphere is typically expected to reduce oxide formation by facilitating the reduction of metal oxides, the increase in oxygen content in this case suggests that the formation of stable ZrO_2 occurred, as this oxide is

thermodynamically stable and difficult to reduce at 700℃. It is likely that at higher annealing temperatures or the use of a more reducing atmosphere would be necessary to reduce the oxide layer effectively.

While EDS was able to provide the elemental composition of the ZrC sample, the technique has limitations when it comes to accurately detecting the presence of carbon in the material. This is because carbon has low energy characteristic X-rays which make them harder to detect.

Table 7.1: Elemental composition of ZrC after ion implantation and annealing at 700℃.

	As-Implanted	Annealed at 700℃
Element	Weight percentage (%)	Weight percentage (%)
Zr	61.60	67.93
C	32.95	10.62
Eu	0.69	1.81
O	4.48	19.34
Ti	0.28	0.30

7.4 X-ray Diffraction (XRD)

Grazing incidence X-ray diffraction (GIXRD) measurements were performed to study the structural changes in the near surface region of the ZrC sample before and after ion implantation. GIXRD measurements were taken again after annealing the ZrC sample at temperatures of 600˚C, 700 ˚C and 800 ˚C. The diffraction patterns were acquired at an incident angle of 5° over the 2θ range of 20-90°.

Figure 7.5 shows the XRD patterns of the virgin, as-implanted and samples annealed from 600℃ to 800℃. The examination of the virgin sample revealed six distinct ZrC crystalline peaks. The sample revealed the presence of (111), (200), (220), (311), (222), and (400) planes at $2\theta°$ of about 33.20, 38.53, 55.63, 66.34, 69.71 and 82.58 respectively. These peaks were matched against the ICDD database card number ZrC-01-073-0477.

Following ion implantation, there was a noticeable reduction in the peak intensity. This decline in peak intensity can be attributed to the damage induced by ion implantation. During ion implantation high energy ions strike the target material and displaces atoms in the crystal lattice of the target. The peaks were fitted, revealing an increase in the FWHM was observed. This observation shows that ion implantation introduces damage into a material. At 2θ of 83, the ZrC phase that was present in the virgin sample had disappeared after ion implantation, this could be due to the damage introduced by implantation.

The implanted sample was then annealed at a temperature of 600˚C, which resulted in change in peak intensity and in peak intensity distribution. This change is attributed to the annealing process which promotes recrystallization of the sample and potential change in grain orientation. The decrease in full width at half maximum (FWHM), which had previously increased due to ion implantation, indicated that recrystallization occurred. The peak observed at 30.12˚ in 2θ° corresponding to the (111) plane was identified to be the main peak of ZrO_2 indicating the temperature at which the oxides start forming. Additionally, recovery of the ZrC peak at 2θ˚ of 83 was observed.

After annealing at 700℃, the ZrO_2 peak intensity increased indicating an increase in wt% of the oxide. The ZrO_2 peaks at 2θ of 30.12, 34.96, 50.22, and 62.68 had reflections corresponding

to (111), (200), (311) and (222) planes. The presence of ZrO_2 confirms the increase in oxygen observed in the EDS data. The increase in oxygen in the EDS analysis initially attributed to the formation of ZrO_2, XRD data confirms this assumption. These peaks were broad, indicating small grains of ZrO_2.

Annealing at 800 ˚C resulted in the reduction of ZrO_2. As mentioned earlier, annealing in hydrogen results in the reduction of oxide formation. The FWHM of the ZrO_2 peak decreased, showing that the broad ZrO_2 peaks that were previously observed, began to narrow. This change suggests an increase in the ZrO_2 grain size. Konnik *et al.* [2] also found that ZrC oxidizes during annealing at high temperatures, forming ZrO_2 and releasing free carbon.

A peak shift was observed at $2\theta°$ of 33.43 and 56.03. After annealing at 700℃, the peak at 33.43° shifted 33.55° while annealing at 800℃ resulted in a shift to 33.47°. Similarly, the peak at 56.03° shifted to 55.86, 56.01 and 56.08 after annealing at 600℃, 700℃ and 800℃ respectively. The observed trend in peak shift could be attributed to the instrument alignment given data collection was on different times. It could also be due to multiple phases present in the sample.

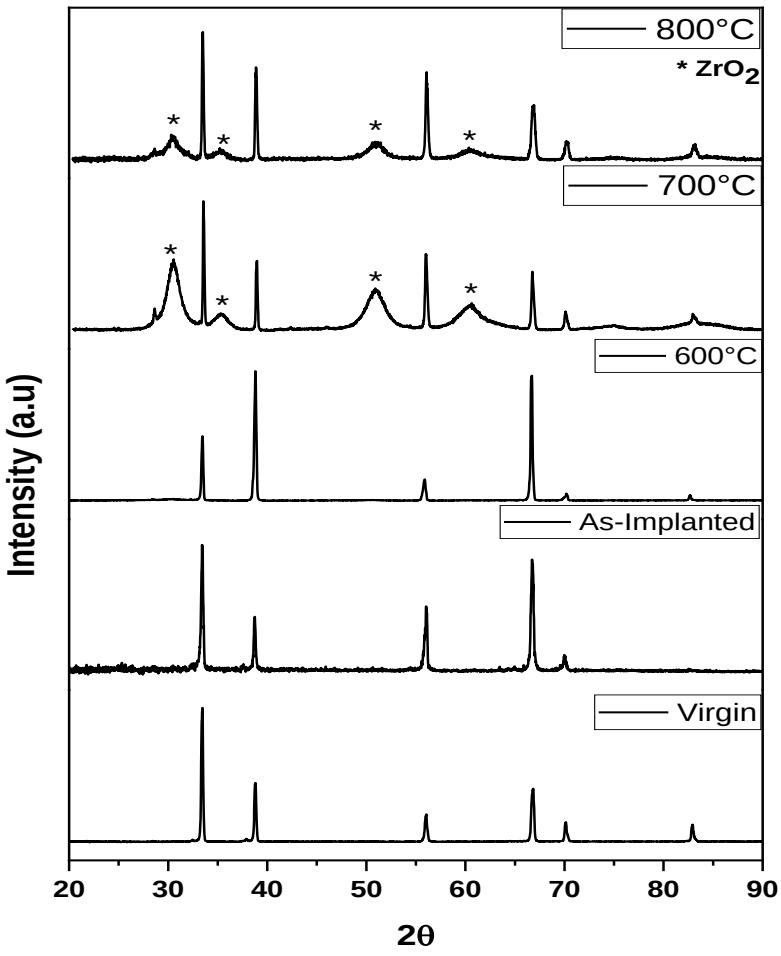

Figure 7.5: XRD pattern of ZrC before, after ion implantation and annealing at 600˚C, 700˚C, 800˚C.

Table 7.2 gives a summary of the phases present in the sample and their respective crystal sizes. The data was obtained using TOPAS software which employs the Rietveld method. From the table, it is observed that the virgin, as-implanted, and 600°C annealed samples were predominantly ZrC. Further annealing resulted in formation of ZrO2 phases. Hydrogen in the annealing environment may have reacted with carbon, leaving a zirconium-rich surface that readily oxidizes. The increased presence of oxides corresponds with the observed rise in oxygen levels from the EDS data.

The crystallite size of the ZrC phases was observed to increase with annealing temperature. This shows that annealing at high temperatures promotes crystallite growth. The crystal size of the ZrO_2 phase decreased as the annealing temperature increased. It is important to note that while high temperature annealing enhances crystal growth, annealing in a hydrogen atmosphere however promotes oxide reduction hence a decrease in the ZrO_2 crystallite sizes is observed. The ZrO_2 broad peaks observed on the XRD pattern of the 700℃ annealed sample are indicative of their small crystallite size.

Table 7.2: Summary of the phases present in the sample and crystal sizes.

Sample description	Crystal size (Å)		Phases (wt%)	
	ZrC	ZrO_2	ZrC	ZrO_2
Virgin	120.1±2.1	26.6±5.5	98	2
As-Implanted	67.3±1.8	9.2±1.8	89	11
Annealed at 600 ˚C	109.6±3.1	5.0±1.1	82	18
Annealed at 700 ˚C	136.8±4.2	5.0±0.1	14	86
Annealed at 800 ˚C	102.4±2.5	5.9±0.1	24	76

The lattice parameter and lattice volume before, after ion implantation and annealing from 600˚C to 800˚C of the ZrC phases were calculated and are shown in table 7.3. The lattice parameters of the samples showed a cubic structure. The lattice parameter (*a*) of the virgin increased after ion implantation from (4.6500733 to 4.6511126). This indicates the sample underwent lattice strain after ion implantation. Annealing at 600˚C, 700˚C and 800˚C resulted

in a decrease in the lattice parameters from 4.6658179 to 4.6599575 then to 4.6464647 respectively.

The lattice volume was observed to follow the same trend, increasing after ion implantation from 100.54938 to 100.61681 and subsequently decreasing from 101.57419 at 600˚C to 101.19193 and 100.31547 at 700˚C and 800˚C respectively. This suggests that initially the sample experiences tensile strain then after annealing it relaxes. It is worth noting that although the sample relaxes upon annealing, overall it remains strained. This is attributed to the fact that the oxide layer is still present. This trend in the lattice parameters and lattice volume indicates that the material experienced non uniform strain.

Table 7.3: Lattice parameter and lattice volume of ZrC.

Sample description	Lattice parameter (Å)	Lattice Volume ($Å^3$)
Virgin	4.6500733	100.54938
As-Implanted	4.6511126	100.61681
Annealed at 600 ˚C	4.6658179	101.57419
Annealed at 700 ˚C	4.6599575	101.19193
Annealed at 800 ˚C	4.6464647	100.31547

The lattice strain and dislocation density were calculated and are shown in table 7.4. The ZrC experienced some level of lattice strain due to ion implantation and formation of the oxide layer emanating from annealing. The calculated lattice strain shows that ion implantation increases the lattice strain while annealing initially relaxes the strain. As the oxide layer grows with further annealing the strain is increased. This could be due to lattice mismatch between ZrC

and ZrO2. Further annealing relaxes the strain. This could be attributed to effect of annealing in a hydrogen atmosphere which promotes oxide reduction.

The dislocation density of ZrC (which is given by the inverse square of the crystal size) increased following implantation. It increased from 6.93×10^{15} to 2.20×10^{16} indicating that the process introduces defects into the material. After annealing, the dislocation density was observed to decrease, from 2.20×10^{16} to 5.11×10^{15} showing that annealing promotes recrystallization. Then suddenly increases, this is due to a similar trend observed in the crystal sizes of the ZrC phases. Dislocation density and crystal size have an inverse relationship.

Table 7.4: Lattice strain and dislocation density.

Sampe description	Lattice Strain	Dislocation density (ZrC)
Virgin	0	6.93×10^{15}
As-Implanted	0,000728	2.20×10^{16}
600˚C	0,000674	8.32×10^{15}
700˚C	0,003363	5.11×10^{15}
800˚C	0,002316	9.52×10^{15}

7.5 Discussion

The results from RBS, XRD, EDS and SRIM simulations provide insights on the behaviour of Eu in ZrC after ion implantation and annealing, shedding light on the mechanisms of surface interaction and ion migration. The SRIM simulations predicted an implantation depth for Eu around 67 nm, with maximum radiation damage closer to the surface at about 40 nm, suggesting that Eu ions would mainly reside near the surface. This depth profile aligns with

RBS data from the as-implanted sample, which observed Eu at a slightly deeper position of approximately 76 nm, a minor difference likely due to the limitations of the SRIM program.

After implantation, XRD analysis showed structural damage in the ZrC lattice, evidenced by increased FWHM, indicating lattice strain and defects. This observation supports the SRIM simulation's indication of damage from displaced ZrC atoms, which is further confirmed by EDS data showing successful Eu incorporation into the ZrC matrix. The lattice parameter increase in XRD suggests tensile strain caused by the presence of Eu ions within the ZrC lattice. However, after annealing the material experiences relaxation. This observation shows that the sample goes through non-uniform strain.

When annealed at 700°C, RBS spectra indicated that Eu migrated toward the surface, showing a broader Eu peak and a shallower distribution. EDS data support this, revealing a higher Eu concentration near the surface after annealing, likely due to thermally driven diffusion. The increase in oxygen content seen in EDS suggests surface oxidation, attributed to Zr's tendency to form ZrO_2, which XRD also confirms with new ZrO_2 peaks after annealing. Additionally, the narrowing of ZrC peaks in XRD and the recovery of certain peaks imply partial recrystallization of the ZrC lattice, healing some implantation-induced damage.

Annealing at 800°C caused further migration of Eu toward the surface, with a marked decrease in Eu within the ZrC matrix, suggesting continued outward diffusion or volatilization. At the same time, XRD indicated reduced ZrO_2 peak intensity, possibly due to partial oxide reduction in the hydrogen annealing atmosphere.

These observations suggest a mechanism where Eu ions, initially implanted near the surface, create lattice strain and damage within ZrC. Thermal annealing activates Eu diffusion towards the surface as atomic mobility increases and the lattice relaxes, while ZrO_2 formation at the surface acts as a barrier, slowing further outward migration. At higher temperatures, some Eu likely volatilizes or migrates further outward. This process provides better understanding of the structural changes, elemental composition, and ion diffusion behaviour of Eu in ZrC.

7.6 References

1. Huang, Z., Zhu, Z., Su, M., Shi, Y., Deng, M., Chen, R., Wang, Z., Zhou, Z., Qi, J. and Wang, H., 2023. High-temperature oxidation behaviors of dense TMC (TM= Ta, Nb, Ti and Zr) ceramics in air. Ceramics International, 49(23), pp.38036-38046.
2. Konnik, M.T., Oldham, T., Rzepka, A., Le Maout, V., Stephani, K.A. and Panerai, F., 2024. High-temperature oxidation and nitridation of substoichiometric zirconium carbide in isothermal air. Journal of the European Ceramic Society, 44(11), pp.6771-6776.

Chapter 8 : Conclusions and Future work

8.1 Conclusions

This study investigated how europium ion implantation and subsequent annealing affect the microstructure of zirconium carbide (ZrC) and influence europium diffusion. To study the microstructural changes, XRD was used, SEM was used to study the surface morphology, EDS examined the elemental composition of the sample, while the diffusion behaviour of europium was investigated using RBS.

SRIM simulation was used to model the behaviour of europium within the ZrC substrate. SRIM simulations predicted a europium penetration depth of approximately 67 nm from the surface. This prediction is consistent with RBS findings, which measured a slightly deeper penetration depth of europium at around 76 nm. The data indicates that the implantation occurred in close proximity to the surface. XRD analysis indicated structural damage due to ion implantation shown by increased FWHM suggesting lattice strain and defects. Thermal annealing introduced notable changes in Eu diffusion and the ZrC matrix.

At 700℃, RBS and EDS data revealed that Eu ions migrated closer to the surface, accompanied by a higher concentration of Eu in this region. This migration was facilitated by thermally driven atomic mobility, and the EDS findings confirmed the localized enrichment of Eu. At 800℃, Eu ions diffused further outward, with RBS spectra showing a broader and shallower distribution. SEM images revealed the presence of larger cracks on the surface of the sample annealed at 800℃, which could have contributed to the continued migration and potential volatilization of Eu ions at higher temperatures.

The oxidation process also played a significant role during annealing. At 600°C, the appearance of ZrO_2 was observed, marking the onset of surface oxidation. By 700°C, XRD analysis revealed distinct ZrO_2 peaks, confirming the growth of oxide layers on the surface, consistent with the increased oxygen content observed in EDS. This behaviour can be attributed to Zr's high affinity for oxygen. At 800℃, XRD revealed narrower ZrO_2 peaks, suggesting partial oxide reduction in the hydrogen-rich annealing atmosphere. These findings illustrate the interplay between ion diffusion, surface oxidation, and atmospheric conditions.

The annealing process also facilitated microstructural recovery in ZrC. XRD data showed enhanced peak intensities and increased crystallite sizes, indicative of recrystallization and improved lattice ordering. This was further supported by a reduction in dislocation density, signifying a decrease in lattice defects caused by implantation. Such structural recovery underscored the potential of thermal treatments to repair implantation-induced damage and restore material integrity.

In summary, this study offers a comprehensive understanding of the structural, compositional and diffusion behaviours of Eu in ZrC following ion implantation and annealing. The findings highlight the critical role of thermal annealing in controlling ion mobility, oxidation and lattice recovery.

8.2 Future work

While this study has provided information about the behaviour of europium (Eu) in zirconium carbide (ZrC) after ion implantation and annealing, several areas remain that still need further investigation:

1. **Long-Term Stability of ZrC in Reactor-Like Conditions**

   Future studies should focus on evaluating the behaviour of Eu-implanted ZrC under conditions mimicking nuclear reactor environments. This includes investigating the behaviour of ZrC after swift heavy ion irradiation, prolonged annealing duration, and varying atmospheric conditions to assess material stability, oxidation resistance, and Eu retention over extended periods.

2. **Influence of Implantation Parameters**

   The role of different ion implantation energies, fluences, and temperatures on the depth profile and lattice interactions of Eu within ZrC needs further investigation. This could reveal how implantation conditions influence damage creation, defect evolution, and ion distribution, enabling the fine-tuning of implantation protocols.

3. **Advanced Characterization Techniques**

   Using more characterization techniques, such as transmission electron microscopy (TEM) for nanoscale defect analysis, atom probe tomography (APT) for 3D elemental mapping, and X-ray absorption spectroscopy (XAS) for oxidation state determination, will assist in providing more information of the microstructural and compositional changes.

4. **Thermomechanical Properties of Eu-Implanted ZrC**

   Investigating changes in the thermomechanical properties, such as hardness, Young's modulus, and thermal conductivity, after implantation and annealing would help evaluate the material's performance under mechanical stress and high temperatures in operational settings.